Particle image velocimetry in a centrifugal pump: Influence of walls on the flow at different axial positions

Rodolfo M. Perissinotto[1]
Center for Energy and Petroleum Studies,
University of Campinas (UNICAMP),
R. Cora Coralina 350, Campinas-SP, Brazil
Email: rodmp@unicamp.br

William D. P. Fonseca
School of Mechanical Engineering,
University of Campinas (UNICAMP),
R. Mendeleyev 200, Campinas-SP, Brazil
Email: fonsecawdp@gmail.com

Rafael F. L. Cerqueira
Mechanical Engineering Department,
Federal University of Santa Catarina,
Rua Roberto Sampaio Gonzaga - Trindade,
Florianópolis, Santa Catarina, Brazil
Email: rafael.cerqueira@ufsc.br

William Monte Verde
Center for Energy and Petroleum Studies,
University of Campinas (UNICAMP),
R. Cora Coralina 350, Campinas-SP, Brazil
Email: wmv@unicamp.br

Antonio C. Bannwart
Center for Energy and Petroleum Studies,
University of Campinas (UNICAMP),
R. Cora Coralina 350, Campinas-SP, Brazil
Email: bannwart@unicamp.br

Erick M. Franklin
School of Mechanical Engineering,
University of Campinas (UNICAMP),
R. Mendeleyev 200, Campinas-SP, Brazil
Email: franklin@fem.unicamp.br

Marcelo S. Castro
School of Mechanical Engineering,
University of Campinas (UNICAMP),
R. Mendeleyev 200, Campinas-SP, Brazil
Email: mscastro@unicamp.br

For almost a century, humans have relied on centrifugal pumps for the transport of low-viscous fluids in commercial, agricultural, and industrial activities. Details of the fluid flow in impellers often influence the overall performance of the centrifugal pump, and may explain unstable and inefficient operations taking place sometimes. However, most studies in the literature were devoted to understanding the flow in the mid-axial position of the impeller, only a few focusing their analysis on regions closer to solid walls. This paper aims at studying the water flow on the vicinity of the front and rear covers (shroud and hub) of a radial impeller to address the influence of these walls on the fluid dynamics. For that, experiments using particle image velocimetry (PIV) were conducted in a transparent pump at three different axial planes, and the PIV images were processed for obtaining the average velocity fields and profiles, as well as turbulence levels. Our results suggest that: (i) significant angular deviations are observed when the velocity vectors on the peripheral planes are compared with those on the central plane; (ii) the velocity profiles close to the border are similar to those in the middle, but the magnitudes are lower close to the hub than to the shroud; (iii) the turbulent kinetic energy on the periphery is up to eight times greater than that measured at the center. Our results bring new insights that can help proposing mathematical models and improving the design of new impellers. A database and technical drawings of the centrifugal pump are also available in this paper, so that other researchers can perform numerical simulations and validate them against experimental data.

Keywords: Particle Image Velocimetry, Centrifugal Pump, Velocity Field

This is a preprint of a paper that will appear in the Journal of Fluids Engineering, https://asmedigitalcollection.asme.org/fluidsengineering

[1]Corresponding Author.

1 INTRODUCTION

Many human activities depend on centrifugal pumps, which are frequently used for the horizontal and vertical transport of liquids in single and multiphase flows. Basically, these devices consist of a rotating component (impeller) that supplies energy to the fluid, and a stationary part (diffuser) that converts part of the kinetic energy into pressure energy [1, 2]. In the particular case of oil production, an electrical submersible pump (ESP) is normally installed inside the oil well to act as an artifical lift method [3, 4].

From the increasing demands of energy saving and long-term operation, the flow structures formed inside impellers and their influence on the pump efficiency have become constant topics of research in the field of fluid mechanics. At off-design conditions, for instance, the flow inside a pump is usually complex due to the presence of unstable structures, engendering high temporal and spatial velocity gradients, regions of intense vorticity and turbulence levels, as well as zones with flow separation, re-circulation and reverse flow. These characteristics directly affect the pump performance and may be a cause of undesirable energy losses [5, 6].

The particle image velocimetry (PIV) technique is non-intrusive, i.e., it does not disturb or modify the flow being investigated [7], therefore the method has proved to be advantageous for carrying out measurements on rotating devices such as stirred tanks, turbines, and pumps. In this context, many researchers worldwide have been using the PIV as a measuring approach to investigate the internal flow in pumps. Paone et al. [8] and Dong et al. [9, 10] were the first to study single-phase flows in a centrifugal pump using PIV. They obtained velocity fields that were analyzed with focus on vorticity and turbulence for describing internal flow patterns and interactions between the volute tongue and the impeller.

As technology applied to lasers, cameras, and computers improved, digital PIV methods became accessible to a larger number of researchers. For instance, Sinha and Katz [11] and Sinha et al. [12] used PIV to investigate the wakes generated by impeller blades, diffuser vanes, and unsteady separation phenomena in centrifugal pumps. Pedersen et al. [13] measured the instantaneous and average velocity fields in a pump working at the design point and low flow rates, and compared the results with data obtained with laser Doppler velocimetry (LDV). Recently, Keller et al. [14] used a PIV system to analyze the unsteady flow field near the volute tongue of a centrifugal pump. For different percentages of the flow rate corresponding to the best efficiency point (BEP), they found that vorticity sheets appear on the surfaces of the impeller blades as a consequence of velocity gradients. Besides, regions with a high turbulent kinetic energy production level were detected in the trailing edge of the blades. These are examples showing that significant attention was devoted to investigate the internal flow in pumps, over the last decades [15–18].

Presently, the studies that rely on PIV techniques to investigate centrifugal pumps are mainly focused on the influence of the flow patterns on hydraulic performance [19–21], presence of vortices or rotating stalls [22–25], and characterization of turbulence levels through the identification of coherent flow structures [26]. These studies, however, cannot evaluate the influence of secondary flows on the general characteristics of the pump's internal flow. Although there are a few studies [14, 27–29] that use the stereoscopic version of the PIV method (2D3C-PIV) to assess the entire volume of fluid in the impeller, most publications available in literature actually rely on the standard two-dimensional PIV (2D2C-PIV) with thin laser sheets that illuminate areas - instead of volumes - of the pump stage. The common configuration of 2D2C-PIV enables the measurements on a plane, so that the velocity is computed in the x and y directions, but not in the z direction. This axial position, z, is usually set up in the middle of the impeller height, far from the solid walls.

This approach was adopted in our previous paper, Perissinotto et al. [5], which described a methodology for applying the 2D2C-PIV in a pump impeller, providing results for the midplane only. Guided by the opportunity to expand our study, we propose the present manuscript, which aims to investigate the flow in different axial positions of the same impeller. This strategy of performing measurements at different axial planes of radial impellers has been recently adopted by Zhang et al. [30] and Ofuchi et al. [31]. Nevertheless, assessing the hub-to-shroud flow behavior is actually a difficulty task, and there is still room to expand this type of analysis in literature. In this sense, we carried out PIV measurements at three axial positions to assess the influence of solid walls on the flow characteristics. In the tests, the laser plane was positioned successively at the impeller center (equidistant from shroud and hub), next to the bottom cover (hub), and next to the top cover (shroud) of the impeller, and single-phase water flows were imposed for different pump rotations.

By analyzing these 3 sets of results (upper, central, lower planes) and comparing them with our previous results (extracted from [5]), we can state that: (i) significant angular deviations are observed when the velocity vectors on the peripheral planes are compared with those on the central plane; (ii) the velocity profiles close to the border are similar to those in the middle, but the magnitudes are lower close to the hub than to the shroud; and (iii) the turbulent kinetic energy on the periphery is up to eight times greater than that measured at the center. These observations help improve the understanding of fluid dynamics within centrifugal pumps, as well as the relationship between the flow behavior and pump performance.

In the following, Section 2 presents the experimental setup, Section 3 discusses the results, and Section 4 finally summarizes the main conclusions.

2 EXPERIMENTAL SETUP

This section describes the experimental setup of the current study, including the test facility (subsection 2.1), PIV system (subsection 2.2), data processing and computations (subsection 2.3).

2.1 Test bench with transparent pump. The test bench used in this work is the same described in Perissinotto et al. [5]. The layout of the experimental facility is depicted in Fig. 1. As can be seen, the setup is essentially composed of a water flow line with a tank, a re-circulation pump, a booster pump, a transparent pump, and a PIV system. Instruments with relative uncertainties lower than 0.5% measure the water flow rate (Q_w) and temperature (T), pressure in the suction point of the transparent pump (P), pressure increment generated by this same pump (ΔP), and rotational speed of its impeller (N). The analog output signals from these instruments are acquired and the measured data monitored and stored by a supervisory control program. During the experiments, Q_w and P are controlled by setting the rotational speed of the booster pump and adjusting the opening or closing level of the valve assembled at the discharge point of the transparent pump. Furthermore, T is kept constant at approximately 25°C by a heat exchanger and thermochiller system.

The transparent centrifugal pump installed in the test bench was also used in Perissinotto et al. [5] and consists of an impeller (closed radial type), a vaneless diffuser (volute type), and other parts such as body, shaft, intake and discharge ports. Details of the design and manufacture are available in Perissinotto et al. [32]. To enable optical measurements using the PIV method, the shroud and blades of the impeller are made of acrylic (or plexiglass), while the hub is made of matte black aluminum. The transparent parts enable the laser sheets to enter and exit the pump while the dark surfaces help reduce undesirable reflections and enhance contrast in the images.

The impeller has a radial geometry based on a real electrical submersible pump (ESP), P23 model, *Centrilift* 538 series, manufactured by *Baker Hughes*. It has seven channels of a constant height h_{imp} = 6 mm, inner diameter d_1 = 44 mm, and outer diameter d_2 = 110 mm, so that the aspect ratio is low, $h_{imp}/d_2 \approx 5\%$. The volute spiral has a radius r_{vol} that varies as a function of the angle, so that $58.5 < r_{vol} < 92.0$ mm. This component has a rectangular cross section with a constant height h_{vol} = 11 mm in the z direction [32]. A photograph of the visualization stage of the transparent pump is displayed in Fig. 2, which highlights the closed radial impeller.

The liquid enters the pump through four intake ports located at the pump body. Then, the fluid reaches the suction eye in the impeller inlet, traverses the channels, and leaves the impeller to be collected by the volute. The liquid is finally directed to the discharge port, placed at the end of the spiral [5]. Subsection 3.4 contains technical drawings of the transparent pump.

2.2 Test matrix and PIV setup. The test matrix for the present study contains six operational conditions, as listed in Tab. 1: two rotational speeds (N) and three flow rates (Q_w) referenced as percentages of the flow rate corresponding to the BEP (Q_{BEP}). This experimental campaign repeats the conditions analyzed by Perissinotto et al. [5] and then allows a more adequate comparison between results. Flow visualization was carried out using a two-dimensional PIV technique, with a system already described in [5]. This system is a time-resolved equipment assembled by *Dantec Dynamics*® that provides an energy of 30 mJ per pulse when working at 1 kHz. In this paper, the laser was set to work at 200 Hz.

As a complement to the information available in Tab. 1, the head curves of the transparent pump operating at both rotational speeds are shown in Fig. 3. The pump head is defined as $H = \Delta P/\rho g$ [33], where ΔP is the pressure generated by the pump, ρ is the water density, g is the modulus of the gravitational acceleration $\vec{g}$. The flow rates investigated in this study are highlighted in these curves, i.e., conditions close to shut-off, BEP, and open-flow. Curves of dimensionless head are available in [5] together with torque measurements and efficiency calculations. However, for the reader's convenience, efficiency curves are also plotted in Fig. 3 to supplement the pump performance information. As it is possible to observe, the efficiency is lower than 10%, as a consequence of the energy dissipation occurring in mechanical elements assembled on the pump shaft, such as bearings and seals, which compose the transmission system of the motor-pump set [5].

During the PIV tests, microspheres of acrylic doped with rhodamine-B dye, with diameters from 20 to 50 μm, are added to water to serve as fluorescent tracers in the scope of laser-induced fluorescence (LIF). However, for low flow rates, these particles tend to deposit at the bottom of the pump stage, over the course of the test. Thus, Q_w = 0.15 m^3/h is the lowest possible flow rate for acquiring adequate images, being considered here as the shut-off point. In addition, the time between two consecutive pulses of the laser generator must be set within the range from 300 to 800 μs to limit the maximum displacement of the particles to 10 pixels in the images [5].

Each experimental condition demands the acquisition of 500 pairs of images in the PIV measurements. A high-speed camera with a spatial resolution of 2560 px × 1600 px is used for capturing these images, having a 0.1 mm/px relation for the the fields of view used in this work. The acquisitions are performed only when the impeller reaches a predetermined angular position, in which the tip of the volute tongue becomes vertically aligned with the tip of a predefined impeller blade. For that, a triggering system is used, consisting of a synchronizer and a rotary encoder assembled on the pump shaft [5] (see Fig. 1).

The illumination planes are positioned perpendicularly to the camera lens, in a configuration that illuminates the entire pump stage (x and y direction) at either of three locations along the impeller height (z direction): (i) on the central plane (equidistant from solid walls); (ii) next to the internal surface of the impeller hub (displaced −3 mm from the center); and (iii) next to the internal surface of the impeller shroud (displaced +3 mm from the center), as observed in Fig. 4. The use of two planes in opposite directions, entering from both sides of the pump, is intended to make the lighting more effective. Eventual shadows caused by the shaft and distortions caused by the blades are mitigated through this double-plane configuration.

Before starting each experiment, the thickness of the laser sheet is set to approximately 1 mm, and the axial position adjusted and confirmed with a dial gauge indicator. The variations in the axial positions of the planes, in the configurations (ii) and (iii), are the most significant difference between the experiments carried out in the present manuscript and those performed before, in Perissinotto et al. [5].

2.3 Data processing and calculations. When the experiment is completed, a pre-processing code is applied to the 500 raw images in order to mask out solid walls, including the blades, where the fluid is not present. Then, a numerical code based on Liu et al. [34] is applied to remove the angular displacement of the impeller between consecutive images. This procedure ensures that the location of the blades is exactly the same in both frames of each pair of images. The images are then sent to a cross-correlation routine carried out on the *DynamicStudio 7.4* software. An adaptive PIV method, as reported by Scarano and Riethmuller [35], with initial and final interrogation regions of 64 px and 32 px and 25% overlap, is responsible for calculating the velocity vectors.

The result is a set of 500 instantaneous velocity fields, and by using an in-house software, these fields are finally converted into a single field of phase-ensemble averaged velocities, as minutely described in Perissinotto et al. [5]. (This amount of 500 images is sufficient to provide fields with satisfactory quality. From preliminary tests, we verified that convergence is achieved when more than 200 images are used in the ensemble-average calculation [5]). In this case, each velocity vector is a relative velocity (**W**) which, by definition, is mathematically equivalent to subtracting the tangential term ($\Omega \times \mathbf{r}$) due to the impeller motion from the absolute velocity (**U**) in the velocity triangle [33]. Thus, the procedure of removing the angular displacement of the impeller is equivalent to calculating the term $\mathbf{U}_i - \Omega \times \mathbf{r}_i$ in the following equation:

$$\langle \mathbf{W} \rangle = \frac{1}{n} \sum_{i=1}^{n} \mathbf{W}_i = \frac{1}{n} \sum_{i=1}^{n} (\mathbf{U}_i - \Omega \times \mathbf{r}_i) \tag{1}$$

where n is the number of images that compose the ensemble-averaged velocity, Ω is the angular velocity, which is proportional to the rotational speed, and $\mathbf{r}$ is the radial position, which varies from the inner to the outer radius in the impeller. Working with relative velocity vectors is convenient especially for regions inside or close to the impeller. The magnitude of this relative velocity can be normalized by the tangential velocity calculated at the tip of the blades, at the impeller outlet, where $r = r_2$. In this case, $W^* = W/(\Omega r_2)$.

Figure 5 illustrates the procedure that transforms raw images from a PIV test into an average field of relative velocity.

For a position (x_i, y_i) in the impeller and an operating condition (N, Q_w) of the pump, the comparison of two different vectors is an interesting strategy to evaluate the influence of the axial position (z) on the flow dynamics. Therefore, a vector found on the periphery (e.g. $\mathbf{W}_{shroud}$) can be compared with a correspondent vector found on the central plane ($\mathbf{W}_{center}$), through a cross product that offers an estimation of the alignment between both vectors, measured by angle ϕ:

$$\phi = \arcsin\left(\frac{\langle \mathbf{W}_{shroud}\rangle}{|\langle \mathbf{W}_{shroud}\rangle|} \times \frac{\langle \mathbf{W}_{center}\rangle}{|\langle \mathbf{W}_{center}\rangle|}\right) \tag{2}$$

The velocity vectors obtained from the PIV tests have components only in the x and y directions, without any values in z. It is thus possible to write $\mathbf{W} = \mathbf{w}_x + \mathbf{w}_y$. Besides, each instantaneous velocity vector can be understood as the sum of an average velocity with a fluctuation in time. From this definition, an analysis of the turbulence levels can be performed in the impeller. Since only two components of the velocity fluctuations are available in the 2D2C-PIV measurements, the turbulent kinetic energy, K_{2D}, is calculated as [14]:

$$K_{2D} = \frac{1}{2}\left(\langle \mathbf{w'}_x\rangle^2 + \langle \mathbf{w'}_y\rangle^2\right) \tag{3}$$

where $\langle \mathbf{w'}_x\rangle^2$ and $\langle \mathbf{w'}_y\rangle^2$ are variances of the velocity fluctuations in time, calculated as: $\langle \mathbf{w'}_x\rangle^2 = \frac{1}{n}\sum_{i=1}^{n}(\mathbf{w}_{x,i} - \langle \mathbf{w}_x\rangle^2)$ and $\langle \mathbf{w'}_y\rangle^2 = \frac{1}{n}\sum_{i=1}^{n}(\mathbf{w}_{y,i} - \langle \mathbf{w}_y\rangle^2)$. The resultant turbulent kinetic energy can be normalized by the linear velocity of the blade tip, $K^*_{2D} = K_{2D}/(\Omega r_2)^2$ [14], where r_2 is the outer radius or half the outer diameter d_2. To improve the quality of instantaneous vectors, we use pre- and post-processing procedures (applying filters, removing invalid vectors, etc). Furthermore, the adaptive PID method is configured to only accept vectors that meet certain criteria (peak height, height ratio, signal-to-noise ratio) and replace, in the last iteration, those that do not meet the minimum requirements.

3 RESULTS AND DISCUSSIONS

This section presents the main results obtained from acquiring and processing PIV images on different axial planes of the transparent pump. Velocity fields (subsection 3.1) and profiles (subsection 3.2) in different positions and conditions, as well as turbulence (subsection 3.3), compose the results discussed here.

3.1 Velocity fields and deviations between vectors. The fields of ensemble-averaged relative velocities measured on the central plane of the impeller, $\mathbf{W}_{center}$ (Eq. 1), are presented in Fig. 6 for the six conditions investigated in this manuscript. The impeller rotates in the clockwise direction.

The relative velocity is very low when the pump operates at low flow rates. In the condition close to shut-off, Figs. 6(a) and 6(b) reveal that the flow topology is characterized by the presence of vortices and reverse flow. This is valid mainly at the left side of the impeller, which is close to the volute tongue and adjacent to the first half of the volute spiral, where r_{vol} is relatively small. Then, at the design point, Figs. 6(c) and 6(d) show that the flow becomes more well-organized and aligned with the curvature of the blades, as expected for the BEP. In the condition corresponding to open-flow, however, Figs. 6(e) and 6(f) indicate that the vectors undergo a deviation toward the suction surface of the blades. The structure becomes similar to half a counterclockwise vortex as the boundary layers tend to detach from the pressure blades. These observations agree with results presented in Perissinotto et al. [5] for other tests focused on the central plane of the impeller.

The magnitude of the relative velocity vectors in Fig. 6 is limited to the range $1.2 < W_{center} < 3.2$ m/s. The velocity at the tip of each blade is $\Omega r_2 = 3.5$ m/s for $N = 600$ rpm and $\Omega r_2 = 5.2$ m/s for $N = 900$ rpm, where $r_2 = d_2/2$ is the outer radius of the impeller. It means that the scale used in W_{center} represents 23% to 69% of the velocity Ωr_2, depending on the condition.

Other velocity fields are presented in Fig. 7, for three flow rates at $N = 600$ rpm. In this case, the velocity is measured on the peripheral laser planes that illuminate the flow next to the hub ($\mathbf{W}_{hub}$) and shroud ($\mathbf{W}_{shroud}$). From a visual inspection of the images, we can observe that there are no major differences between the central and peripheral flow fields. However, divergences exist, and become more evident when streamlines are analyzed together with the velocities.

Thus, Fig. 8 compares the streamlines obtained on the three planes, for each flow rate Q at the rotational speed $N = 600$ rpm. These streamlines are superimposed on contour plots of the relative velocity, W, normalized by the tangential velocity due to the impeller rotation, Ωr, calculated on the tip of the blades at the impeller exit, r_2. Therefore, the plots contain values of $W^* = W/(\Omega r_2)$, as explained in subsection 2.3.

An evaluation of the alignment between vectors is another way of highlighting the differences between these velocity fields. The idea is to calculate the angle ϕ (Eq. 2) between the peripheral and central velocity vectors in each position of the two-dimensional field. The contour plots from Fig. 9 highlight the regions where the vectors are most misaligned. At shut-off conditions, deviations occur due to variations in the position of the vortices, as depicted in Figs. 9(a) and 9(b), in which $-90° < \phi < 90°$. At the BEP, the most relevant deviations are found in the upper left channels, where the angles are limited to the scale $-60° < \phi < 60°$, as shown in Figs. 9(c) and 9(d). Then, at the open-flow condition, the changes in the vectors are concentrated mainly on the pressure blades, as depicted in Figs. 9(e) and 9(f), with deviations in the range $-60° < \phi < 60°$.

The analysis was extended for $N = 900$ rpm in Fig. 10 and we note that the results are similar to those obtained at $N = 600$ rpm. The main differences include the positions of vortex structures at the lowest water flow rate. In addition, at the BEP, the blue regions where $\phi > 60°$ in Fig. 9(c) disappear when N increases, as can be seen in Fig. 10(c). Such characteristics are probably related to the dynamics of the water flow. However, we analyzed the raw PIV images and observed that: 1) For flow rates close to the shut-off, part of the tracer particles tend to segregate and deposit in the lower regions of the pump, so that there is a lack of particles on the images; 2) At the BEP, some particles accumulate in the vicinity of the blades, giving rise to white spots in the images. These situations have possibly impaired the quality of the image processing, despite our attempts to minimize the issues by applying pre- and pos-processing techniques. Yet, it is worth mentioning that the clearance leakage becomes more severe as the rotational speed increases, so that the flow rate measured by the flow meter becomes different from the actual flow rate in the impeller. This fact may cause some influence in the fields obtained at different N.

For both N, the deviations between vectors are more significant near the hub than near the shroud. We should remember that the shroud is made of polymeric material (acrylic), while the hub is made of metallic material (aluminium) with a layer of paint. These parts have different surface roughness, which may affect the flow behavior. In addition, another important feature that influences the flow is the geometry of the pump prototype regarding the assembly of the closed radial impeller inside the vaneless volute diffuser. The hub faces the rear part of the pump stage, while the shroud is spaced 2 mm away from the front part, due to the presence of a gap downstream from the impeller.

This detail of the visualization section is shown in Fig. 11. The flow encounters an "opening" as it leaves the impeller next to the internal surface of the shroud. The fluid is free to move towards the front cover of the volute, configuring a three-dimensional mean flow, with a velocity term in the z direction. On the other hand, when exiting close to the hub surface, the flow continues adjacent to the solid walls. The impeller hub is mounted at the same height as the volute bulkhead, that is, these parts have identical dimensions in the z direction.

Differences between the flow in the shroud and the flow in the hub are also a consequence of the geometry of components placed upstream from the impeller. They possibly cause the flow to change its direction as it enters the channels. This effect will be discussed in subsection 3.2.

3.2 Velocity profiles. The current subsection aims to discuss the differences between the velocity profiles obtained on the three axial planes of the impeller. These profiles are thus evaluated at three radial positions $r = [27, 38, 50]$ mm, which correspond to $r^* = r/r_2 = [0.5, 0.7, 0.9]$ when normalized by the outer radius of the impeller. The analysis is focused on two channels: CA is far from the volute tongue, while CB is very close to it. The exact location of CA and CB can be defined as follows: CA is the only channel whose entrance is completely within the first quadrant of the impeller; CB is the only channel whose exit is completely within the third quadrant of the impeller.

Each channel is defined by a circumferential position, c, which can be normalized. In this case, $c^* = 0.0$ refers to the suction surface of the blade (SB) and $c^* = 1.0$ corresponds to the pressure surface (PB), where $c^* = (c - c_{SB})/(c_{PB} - c_{SB})$. Examples of velocity profiles determined at the central plane are available in Fig. 12 for the shut-off, BEP, and open-flow conditions at $N = 600$ rpm. The figure also highlights the three radial positions r^*, the circumferential direction c, and the location of channels CA and CB.

Figures 13, 14 and 15 compare the profiles acquired on the central plane (according to Fig. 12) with the ones measured on the peripheral planes (i.e., next to hub or shroud), for $N = 600$ rpm, at flow rates associated with the shut-off, BEP, and open-flow conditions, respectively. The y-axis of the graphs contains the magnitude of the relative velocity normalized by the tangential velocity at the impeller exit, $W^* = W/(\Omega r_2)$, as explained in subsection 2.3.

As a general rule, the ensemble-averaged relative velocity increases as the flow rate increases. However, for a constant flow rate, this velocity tends to decrease as the radial position changes from the inner ($r_1^* = 0.5$) to the outer region ($r_3^* = 0.9$). This fact is related to the geometry of the channel, which is similar to a divergent nozzle – in other words, as the radial position increases, the cross-sectional area of the channel also increases, so that the velocity decreases for a fixed flow rate. Furthermore, the velocity tends to have higher magnitudes in channel CA than in channel CB. This behavior is a consequence of the interaction between the impeller and volute, as the solid walls that compose the volute spiral influence the flow in the impeller channels [5].

From Figs. 13, 14 and 15, we observe that the relative velocity on the peripheral planes is similar to that on the central plane. In most conditions, the curves for W and W^* present the same shape, independently of the axial position of the plane illuminated during the PIV tests. For the lowest flow rate, differences are detected in channel CB (Figs. 13(b), 13(d), 13(f)). The curves appear to be translated relatively to each other, as if there was a phase shift between the peaks and valleys. This result is possibly associated with the position of vortex structures, which vary slightly as a function of the plane considered (see Fig. 8(a)).

At the BEP, the curves for channel CB (Figs. 14(b), 14(d), 14(f)) reveal that the velocity has a lower intensity on the hub plane than on the other planes. We observe the same trend in channels CA and CB at the highest Q_w (Fig. 15). In fact, such differences are probably an effect of the surface finish, as the hub has a larger roughness than the shroud, because the former is a machined aluminum part whereas the latter is a polished acrylic plate. There is possibly a relationship between the flow fields in the impeller and the material used in its manufacture. This fact could be further explored by the industry in the search for more efficient impellers.

Nevertheless, at the highest flow rate (Fig. 15) most velocities measured on the shroud plane (close to the walls) are higher than the ones measured on the central plane (far from the walls). We should remember that the flow in the impeller is also influenced by the geometry of the other components mounted in the centrifugal pump. Before entering the impeller, the fluid undergoes a change in its direction, which causes a deviation in the streamlines towards the internal surface of the shroud, especially at high flow rates. As a result, the velocity profiles become more distorted.

This is illustrated in Fig. 16. In the drawing, the yellow component is a diffuser adapted from the ESP P23 model. Its purpose is to guide the fluid into the impeller, reducing the occurrence of collisions with the solid walls [32]. However, although the part smooths out the change in the flow direction, it still happens, on a 180° curve.

The profiles drawn in Fig. 16 were inspired on an analogy between pumps and ducts. Inside a pipeline, a considerable length is required after a bend for the flow to recover its full development. In fact, the flow in a tight bend is characterized by distorted velocity profiles with the occurrence of different secondary flow patterns depending on the transverse and longitudinal locations [36–38]. An even worse condition is expected in the impeller, as the geometry is complex (curved channel with a variable cross-sectional area) and the distances are short (just a few millimeters from inner to outer radius). This would be another opportunity for improvements in the design of commercial pumps: the components located upstream from the impeller may be modified to beneficially influence the flow behavior and the efficiency of energy transfer in the impeller.

We extended the analysis for N = 900 rpm and obtained similar results. The curves of relative velocity present similar shapes for both rotational speeds, but the magnitudes increase as N rises. Thus, the observations made for N = 600 rpm are also valid for N = 900 rpm, and other graphs will be suppressed because they do not provide new information to the discussions.

3.3 Turbulent kinetic energy.

The turbulent kinetic energy, K_{2D}, is a measure of the energy associated with velocity fluctuations in time. It is thus calculated from the variances $\langle \mathbf{w'}_x \rangle^2$ and $\langle \mathbf{w'}_y \rangle^2$ in the x and y directions (Eq. 3), obtained by subtracting the average from the instantaneous velocity vectors in each interrogation window of the PIV fields. Figure 17 shows the turbulent kinetic energy computed in the pump stage at $N = 600$ rpm, for three flow rates and three axial positions of the laser planes. The values are normalized by the linear velocity of the blade tip. Hence, $K^*_{2D} = K_{2D}/(\Omega r_2)^2$, in accordance with subsection 2.3.

In Fig. 17, the turbulent kinetic energy evaluated on the central plane agrees well with results from Perissinotto et al. [5]. The K^*_{2D} levels are the lowest when the pump works under the best efficiency point (Fig. 17(*b*)), but they become much more intense when the device operates at off-design conditions (Figs. 17(*a*) and 17(*c*)). Besides, Fig. 17 reveals that the turbulent kinetic energy is higher on the peripheral planes than on the central plane. This is an effect of the interaction between the fluid and solid walls, characterized by significant velocity gradients and shear stresses, which increase the turbulence production and thus make K_{2D} more intense. As we can observe, the contour plots related to the hub and shroud present large areas covered by red spots, revealing large regions where K^*_{2D} is higher than the limits of the scales. Furthermore, it is important to remember that the flow is affected by the parts placed upstream the impeller, as explained in the subsection above (see Fig. 16). In addition to influencing the average velocity profile, it is possible that the component installed behind the impeller also modifies the velocity fluctuations, applied in the K_{2D} calculation.

Another interesting result is the turbulence level within the volute spiral. By comparing the contour plots, we observe that K^*_{2D} in the volute is higher on the hub and lower on the shroud plane. This fact is related to the geometry of the pump stage. As explained in subsection 3.1, Fig. 11, there is a gap (2 mm) between the external surface of the shroud and front cover of the pump stage. As a consequence, the laser plane that illuminates the internal surface of the shroud is almost 5 mm away from the solid walls of the volute. We can thus expect that the K^*_{2D} values are relatively lower in this case, as the velocity gradient and shear stress tend to decrease in locations far from walls.

As stated in the last paragraphs, the turbulent kinetic energy is evaluated from velocity fluctuations measured in each interrogation window of the PIV images. Hence, the sum of each K_{2D} value, in each one of the n_{IW} windows, express an estimation of the total energy associated with turbulence in the entire impeller:

$$K_{2Dsum} = \sum_{i=1}^{n_{IW}} K_{2D} \tag{4}$$

An analysis of the total turbulent kinetic energy was conducted and the results are presented in Fig. 18, for $N = 600$ rpm. The y-axis contains K^*_{2Dsum}, which is normalized by K_{2Dsum} on the central plane, at the BEP. As this condition (BEP on central plane) has the lowest turbulent levels, it is considered here as the reference for comparisons, corresponding to the basic unity of normalized values.

From Fig. 18, we can observe that the total turbulent kinetic energy computed on the peripheral planes reaches values eight times greater than K^*_{2Dsum} measured on the central plane. For a more complete analysis, additional experiments were performed at flow rates corresponding to 30%, 80%, and 120% of the BEP. The data plotted on the graph is adjusted by polynomial fits, following the procedure firstly proposed in Perissinotto et al. [5]. The lowest points of these curves occur around the BEP, while the highest points are found at the conditions furthest from the BEP, i.e., shut-off and open-flow.

The investigations were repeated for N = 900 rpm. We could note that the results are roughly the same as those for N = 600 rpm. Hence, the observations made for the lowest rotational speed are also valid for the highest one. Results for N = 900 rpm will be thus suppressed as they do not include any new information to the discussions developed here.

3.4 Database for future studies. The experimental data acquired in the tests is available at https://gitlab.com/perissinotto/PIV_pump_planes for download. The database contains quantities such as average velocities, velocity fluctuations, and turbulent kinetic energy as a function of the x, y position of the centrifugal pump, measured at different rotational speeds and flow rates, according to the test matrix of this manuscript. Thus, the results for N = 900 rpm (that were suppressed in the last subsections) are included in the folder as well.

Furthermore, the path https://gitlab.com/perissinotto/PIV_pump_planes contains the 3D technical drawings created during the design of the transparent centrifugal pump. These files were originally elaborated on the CAD software *SolidEdge*, academic version, by Siemens. Other two file extensions (IGS and STP) are also provided in the repository for the user's convenience.

Our intention with sharing these files is to allow other researchers to validate the accuracy and fidelity of their models against our experimental data. In this context, the technical drawings of our pump can be used to generate computational meshes and carry out numerical simulations. This may lead to future collaborative studies between diverse research groups.

4 CONCLUSIONS

In this manuscript, experiments using particle image velocimetry (PIV) were carried out to study the single-phase water flow in the closed radial impeller and vaneless volute diffuser of a centrifugal pump. The processed images provided information on the velocity fields, velocity profiles, and turbulence levels in three different axial planes of the impeller: i) a central plane equidistant from the front and rear covers; ii) a peripheral plane adjacent to the internal surface of the front cover (shroud); iii) a peripheral plane adjacent to the internal surface of the rear cover (hub). After analyzing the results and comparing them with literature [5], we can conclude that:

1. The ensemble-averaged relative velocity in the impeller is very dependent on the flow rate (Q). At low Q, close to the shut-off, the flow topology is characterized by the presence of vortex structures that partially block the channels. At the best efficiency point (BEP), the flow is well-organized, with streamlines following the blade curvature. At high Q, close to the open-flow, the streamlines are diverted towards the suction side of the blades, so that the fluid path becomes longer and detached from the pressure blades. These results are valid for the two rotational speeds (N) and three axial planes investigated here. This close connection between flow field and flow rate in the impeller is a consensus among current researchers, so that our observations completely agree with results from other studies available in literature.

2. Significant differences are observed when we compare the velocity vectors on the central plane with those on the peripheral planes. These divergences are identified as angular deviations between two vectors placed at the same x, y point

on two different planes. The misalignment is more relevant on the hub plane due to geometrical attributes of the centrifugal pump: i) a higher roughness of the hub in comparison with the shroud; ii) the existence of a gap between the shroud and the front cover of the volute, which may influence the flow within the impeller. Under the shut-off, the deviations are even more evident, because there are slight variations in the position of vortex structures depending on the plane investigated. However, the deviations under BEP and open-flow conditions do not have a well-defined behavior: there are regions on the peripheral plane in which the vectors have positive (clockwise) deviations in relation to vectors in the central plane; but there are other regions in which this deviation is negative (counterclockwise). Such interesting variations can be confirmed by analyzing the streamlines and velocity profiles.

3. As a consequence of the above conclusions, the velocity profiles are dependent on Q and also on the radial (r) and circumferential (c) positions. Regarding the magnitude of the ensemble-averaged relative velocity, it is possible to observe that this velocity is generally lower on the hub plane and higher on the shroud plane. This is an effect of: i) once again, the surface finish, with a higher roughness on the hub than on the shroud; ii) the influence of other components mounted upstream from the impeller, which smoothly guide the flow, but may favor the deflection of the fluid towards the internal surface of the shroud. The same findings are valid for both N. However, different results may be obtained if the geometry of the pump is modified and its internal components replaced, and this could be an opportunity for future studies.

4. On the central plane, as expected, the turbulent kinetic energy measured at the shut-off and open-flow presents higher values than that one evaluated at BEP, this result being well-known to scholars. The turbulence levels are more relevant: i) at the impeller-volute boundary, where there are significant velocity differences, for shut-off; ii) at the tip of the blades, due to wakes formed at the trailing edges, for BEP; iii) on the pressure side of the blades, where boundary layer detachment occurs, for open-flow. In addition, the turbulent kinetic energy is higher on the peripheral planes, as the presence of walls tends to make the intensity of velocity fluctuations increase. A measure of the total turbulence across the impeller provides values eight times greater on the periphery (shroud plane, open-flow) when compared to the center (mid-axial plane, BEP).

The observations made in this study contribute to a better understanding of the flow subject to the rotating conditions found in a pump impeller. The findings indicate possible points of improvement in the design of centrifugal pumps, such as the reduction of surface roughness and the addition of elements to homogenize the flow. From the availability of the PIV database and technical drawings of the transparent pump, it is expected that new studies can continue this investigation, with the proposition of phenomenological models or execution and validation of numerical simulations, for example.

Suggestions for future studies include: i) Carry out new experiments using time-resolved PIV to further explore the relationship between the characteristics of velocity distribution in different planes and the complex flow phenomena occurring in pump impellers, such as rotational stalls; ii) Expand the investigations for fluids more viscous than water, such as glycerol or mineral oil, to address the effects of viscosity on the flow behavior; iii) Try new impeller designs to investigate the flow characteristics as a function of impeller diameter, blade curvature, number of channels, among others.

Nomenclature / List of Symbols

Symbol	Description
Q_w	Water flow rate
Q_{BEP}	Water flow rate at BEP
ρ	Water density
T	Temperature at pump intake
P	Pressure at pump intake
ΔP	Pressure increment produced by pump
N	Rotational speed of pump impeller
Ω	Angular speed of pump impeller
H	Pump head
d_1, d_2	Impeller inner and outer diameters
r_1, r_2	Impeller inner and outer radii
h_{imp}	Impeller height
r_{vol}	Radius of volute spiral
h_{vol}	Height of volute spiral
$\mathbf{U}$	Absolute velocity vector
$\mathbf{W}$	Relative velocity vector
$\langle\mathbf{W}\rangle$	Average relative velocity vector
W	Relative velocity
W^*	Normalized average relative velocity
$\langle \mathbf{w'}_x \rangle^2, \langle \mathbf{w'}_y \rangle^2$	Variances of velocity fluctuations
ϕ	Angle of deviation between velocity vectors
K_{2D}	Turbulent kinetic energy
K^*_{2D}	Normalized turbulent kinetic energy
K_{2Dsum}	Sum of K_{2D} values throughout the contour plot
K^*_{2Dsum}	Normalized K_{2Dsum}
x, y	Position in Cartesian coordinates
r, c	Position in polar coordinates
r^*, c^*	Normalized radial and circumferencial positions
n	Number of images in the dataset
n_{IW}	Number of interrogation windows in the image

Acknowledgment

We gratefully acknowledge the support of EPIC - Energy Production Innovation Center, hosted by the University of Campinas (UNICAMP) and sponsored by FAPESP – The São Paulo Research Foundation (Process Number 2017/15736-3). We also thank FAPESP for providing the PIV system used in this research through the Multi-User Equipment program (Process Number 2019/20870-6). We acknowledge the support of ANP (Brazil's National Oil, Natural Gas and Biofuels Agency) through the R&D levy regulation. The acknowledgments are also extended to Center for Energy and Petroleum Studies (CEPETRO), School of Mechanical Engineering (FEM), and ALFA Research Group.

References

[1] Stepanoff, A. J., 1957, *Centrifugal and axial flow pumps: theory, design, and application*, Wiley.

[2] Petermann, H. and Pfleiderer, C., 1964, *Strömungsmaschinen*, Springer.

[3] Flatern, R., 2015, "The defining series: electrical submersible pumps," Oilfield Review, pp. 1–2.

[4] Takacs, G., 2017, *Electrical submersible pumps manual: design, operations, and maintenance*, Gulf Professional Publishing.

[5] Perissinotto, R. M., Cerqueira, R. F. L., Fonseca, W. D. P., Monte Verde, W., Biazussi, J. L., Bannwart, A. C., Franklin, E. M., and Castro, M. S., 2023, "Particle image velocimetry in a centrifugal pump: details of the fluid flow at different operation conditions," Flow Measurement and Instrumentation, **89**, p. 102282.

[6] Fonseca, W. D. P., Cerqueira, R. F. L., Perissinotto, R. M., Monte Verde, W., Castro, M. S., and Franklin, E. M., 2023, "Particle image velocimetry in the impeller of a centrifugal pump: a POD-based analysis (no prelo)," Flow Measurement and Instrumentation.

[7] Perissinotto, R. M., Verde, W. M., Biazussi, J. L., Bulgarelli, N. A. V., Fonseca, W. D. P., de Castro, M. S., de Moraes Franklin, E., and Bannwart, A. C., 2021, "Flow visualization in centrifugal pumps: A review of methods and experimental studies," Journal of Petroleum Science and Engineering, **203**, p. 108582.

[8] Paone, N., Riethmuller, M., and Van den Braembussche, R., 1989, "Experimental investigation of the flow in the vaneless diffuser of a centrifugal pump by particle image displacement velocimetry," Experiments in Fluids, **7**(6), pp. 371–378.

[9] Dong, R., Chu, S., and Katz, J., 1992, “Quantitative visualization of the flow within the volute of a centrifugal pump. Part A: Technique,” Journal of Fluids Engineering, **114**(1), pp. 390–395.

[10] Dong, R., Chu, S., and Katz, J., 1992, “Quantitative visualization of the flow within the volute of a centrifugal pump. Part B: results and analysis,” Journal of Fluids Engineering, **114**(1), pp. 396–403.

[11] Sinha, M. and Katz, J., 2000, “Quantitative visualization of the flow in a centrifugal pump with diffuser vanes—I: on flow structures and turbulence,” Journal of Fluids Engineering, **122**(1), pp. 97–107.

[12] Sinha, M., Pinarbasi, A., and Katz, J., 2001, “The flow structure during onset and developed states of rotating stall within a vaned diffuser of a centrifugal pump,” Journal of Fluids Engineering, **123**(3), pp. 490–499.

[13] Pedersen, N., Larsen, P. S., and Jacobsen, C. B., 2003, “Flow in a centrifugal pump impeller at design and off-design conditions—part I: particle image velocimetry (PIV) and laser Doppler velocimetry (LDV) measurements,” Journal of Fluids Engineering, **125**(1), pp. 61–72.

[14] Keller, J., Blanco, E., Barrio, R., and Parrondo, J., 2014, “PIV measurements of the unsteady flow structures in a volute centrifugal pump at a high flow rate,” Experiments in Fluids, **55**(10), pp. 1–14.

[15] Krause, N., Pap, E., and Thévenin, D., 2006, “Investigation of off-design conditions in a radial pump by using time-resolved-PIV,” *Proceedings of the 13th International Symposium on Applications of Laser Techniques to Fluid Mechanics*, Citeseer, pp. 1–11.

[16] Ullum, U., Wright, J., Dayi, O., Ecder, A., Soulaimani, A., Piché, R., and Kamath, H., 2006, “Prediction of rotating stall within an impeller of a centrifugal pump based on spectral analysis of pressure and velocity data,” *Journal of Physics: Conference Series*, Vol. 52, IOP Publishing, Paper No. 1, p. 36.

[17] Westra, R., Broersma, L., van Andel, K., and Kruyt, N. P., 2010, “PIV measurements and CFD computations of secondary flow in a centrifugal pump impeller,” Journal of Fluids Engineering, **132**(6), p. 061104.

[18] Dazin, A., Cavazzini, G., Pavesi, G., Dupont, P., Coudert, S., Ardizzon, G., Caignaert, G., and Bois, G., 2011, “High-speed stereoscopic PIV study of rotating instabilities in a radial vaneless diffuser,” Experiments in Fluids, **51**, pp. 83–93.

[19] Li, X., Chen, B., Luo, X., and Zhu, Z., 2020, “Effects of flow pattern on hydraulic performance and energy conversion characterisation in a centrifugal pump,” Renewable Energy, **151**, pp. 475–487.

[20] Li, X., Chen, H., Chen, B., Luo, X., Yang, B., and Zhu, Z., 2020, “Investigation of flow pattern and hydraulic performance of a centrifugal pump impeller through the PIV method,” Renewable Energy, **162**, pp. 561–574.

[21] Chen, B., Li, X., and Zhu, Z., 2022, “Investigations of energy distribution and loss characterization in a centrifugal impeller through PIV experiment,” Ocean Engineering, **247**, p. 110773.

[22] Wang, Y., Yang, H., Chen, B., Gao, P., Chen, H., and Zhu, Z., 2019, “Analysis of vortices formed in flow passage of a five-bladed centrifugal water pump by means of PIV method,” AIP Advances, **9**(7), p. 075011.

[23] Feng, J., Ge, Z., Yang, H., Zhu, G., Li, C., and Luo, X., 2021, “Rotating stall characteristics in the vaned diffuser of a centrifugal pump,” Ocean Engineering, **229**, p. 108955.

[24] Liu, X.-D., Li, Y.-J., Liu, Z.-Q., and Yang, W., 2022, “Dynamic Stall Inception and Evolution Process Measured by High-Frequency Particle Image Velocimetry System in Low Specific Speed Impeller,” Journal of Fluids Engineering, **144**(4), p. 041504.

[25] Liu, X.-D., Li, Y.-J., Liu, Z.-Q., Yang, W., and Tao, R., 2022, “Dynamic evolution process of rotating stall vortex based on high-frequency PIV system in centrifugal impeller,” Ocean Engineering, **259**, p. 111944.

[26] Chen, B., Li, X., and Zhu, Z., 2022, “Time-Resolved Particle Image Velocimetry Measurements and Proper Orthogonal Decomposition Analysis of Unsteady Flow in a Centrifugal Impeller Passage.” Design, Simulation and Optimization of Hydraulic Machinery, **9**, p. 836456069.

[27] Yang, H., Xu, H., and Liu, C., 2012, “Flow measurements in a model centrifugal pump by 3-D PIV,” *IOP Conference Series: Earth and Environmental Science*, Vol. 15, IOP Publishing, Paper No. 6, p. 062053.

[28] Mittag, S. and Gabi, M., 2016, “Experimental investigation on pump-intake-elbow systems using refraction index matching and TR-SPIV,” *16th International Symposium on Transport Phenomena and Dynamics of Rotating Machinery*.

[29] Shigemitsu, T., Ogawa, Y., and Nakaishi, E., 2019, “PIV measurement of internal flow in mini centrifugal pump,” International Journal of Fluid Machinery and Systems, **12**(4), pp. 251–260.

[30] Zhang, Q., Xie, Z., Kang, S., and Zhang, W., 2022, “Experimental study on fiber suspension in a centrifugal pump by PIV,” *Journal of Physics: Conference Series*, Vol. 2217, IOP Publishing, Paper No. 1, p. 012016.

[31] Ofuchi, E. M., Stel, H., Mancilla, E., and Morales, R. E., 2023, “Investigation of the flow field in a centrifugal rotor through particle image velocimetry,” Experimental Thermal and Fluid Science, **140**, p. 110768.

[32] Perissinotto, R. M., Fonseca, W. D. P., Cerqueira, R. F. L., Monte Verde, W., Biazussi, J. L., Castro, M. S., and Bannwart, A. C., 2022, “Development of a transparent pump prototype for flow visualization purposes,” *Proceedings of Rio Oil & Gas Expo and Conference*, Brazilian Petroleum and Gas Institute.

[33] Gülich, J. F., 2008, *Centrifugal pumps*, Vol. 2, Springer.

[34] Liu, X.-D., Liu, Z.-Q., Zhong, Q., Li, Y.-j., and Yang, W., 2021, “Experimental investigation of relative velocity field based on image rotation method in pump impeller,” Flow Measurement and Instrumentation, **82**, p. 102061.

[35] Scarano, F. and Riethmuller, M. L., 1999, “Iterative multigrid approach in PIV image processing with discrete window offset,” Experiments in Fluids, **26**(6), pp. 513–523.

[36] Yuki, K., Hasegawa, S., Sato, T., Hashizume, H., Aizawa, K., and Yamano, H., 2011, "Matched refractive-index PIV visualization of complex flow structure in a three-dimentionally connected dual elbow," Nuclear Engineering and Design, **241**(11), pp. 4544–4550.
[37] Kalpakli Vester, A., Sattarzadeh, S. S., and Örlü, R., 2016, "Combined hot-wire and PIV measurements of a swirling turbulent flow at the exit of a 90° pipe bend," Journal of Visualization, **19**, pp. 261–273.
[38] Dutta, P., Chattopadhyay, H., and Nandi, N., 2022, "Numerical studies on turbulent flow field in a 90 deg pipe bend," Journal of Fluids Engineering, **144**(6), p. 061104.

List of Tables

List of Figures

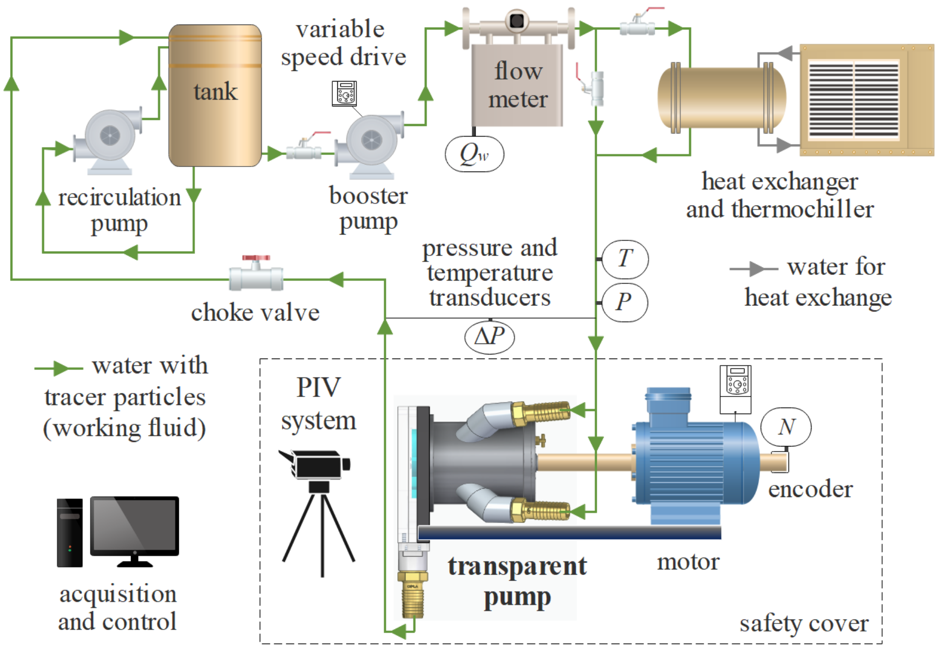

Fig. 1 Layout showing the main components of the test facility.

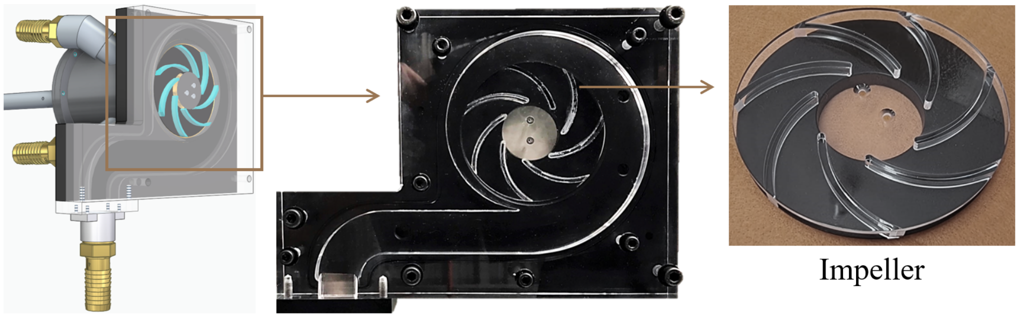

Fig. 2 Visualization section of the transparent pump with impeller and volute.

Table 1 Test matrix with six operating conditions.

	Q_w - absolute and relative to Q_{BEP}		
N	**≤10%**	**∼100% (BEP)**	**∼160%**
600 rpm	0.15 m^3/h	1.5 m^3/h	2.4 m^3/h
900 rpm	0.15 m^3/h	2.2 m^3/h	3.6 m^3/h

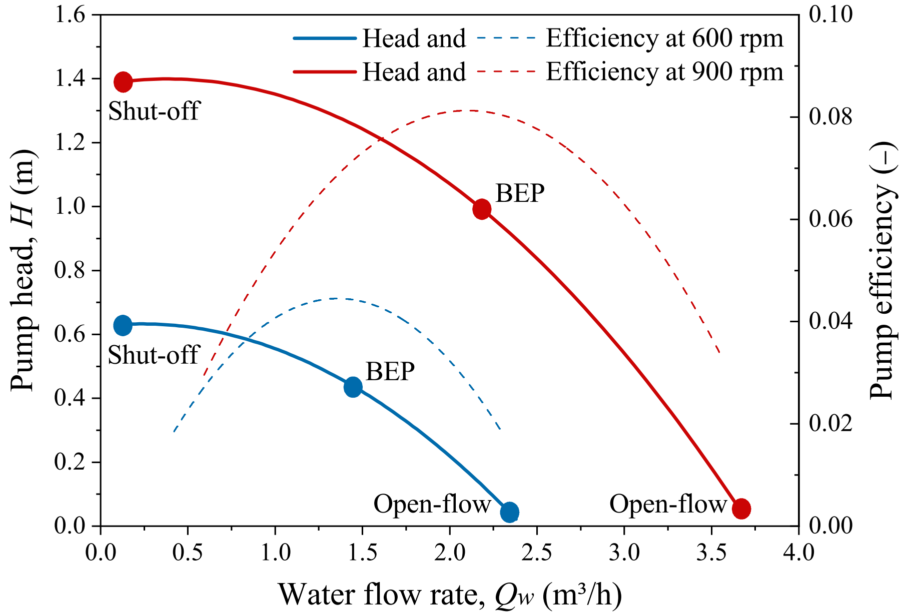

Fig. 3 **Head and efficiency curves of the transparent pump operating with water.**

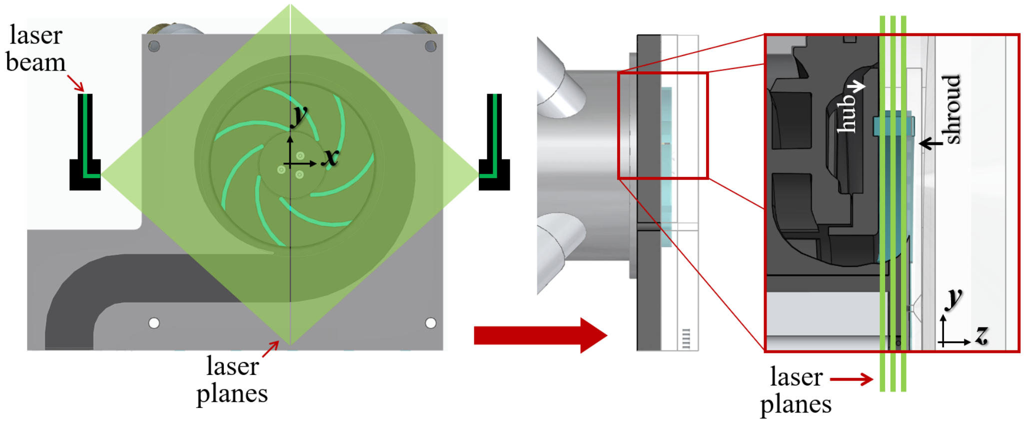

Fig. 4 Configuration of the two laser planes in three axial positions (*z* direction).

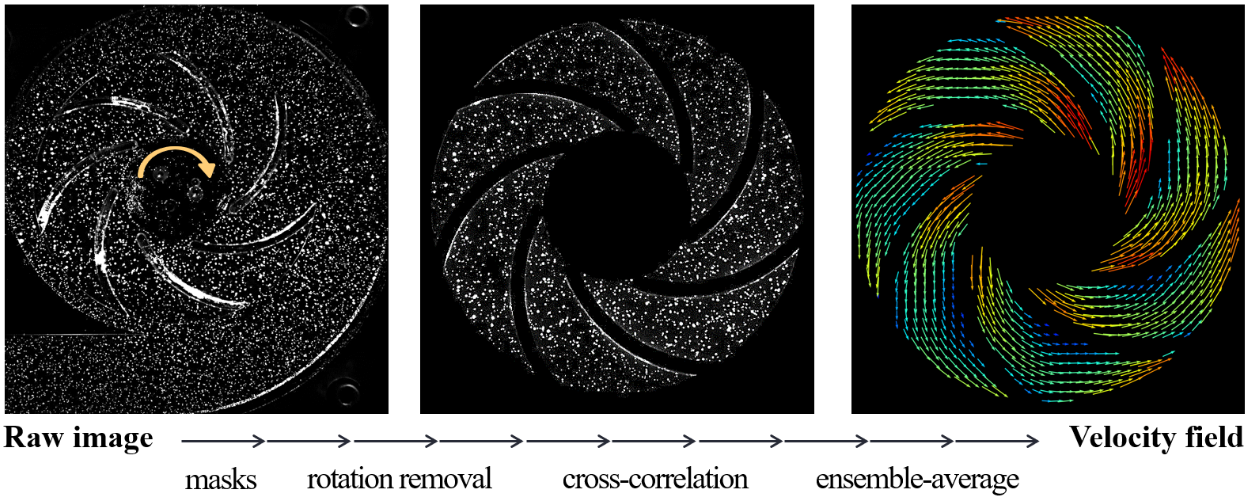

Fig. 5 Illustration of image processing: from raw images to a velocity field.

(a) Q_w = 0.1 Q_{BEP} at N = 600 rpm

(b) Q_w = 0.1 Q_{BEP} at N = 900 rpm

(c) Q_w = 1.0 Q_{BEP} at N = 600 rpm

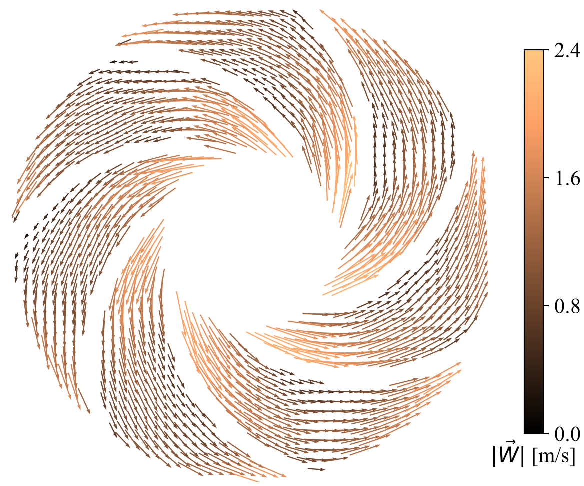

(d) Q_w = 1.0 Q_{BEP} at N = 900 rpm

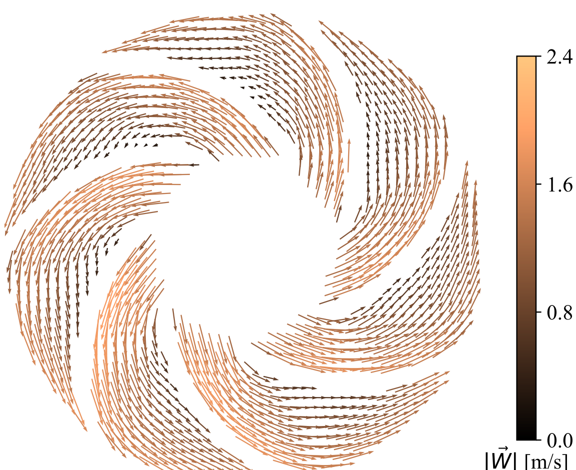

(e) Q_w = 1.6 Q_{BEP} at N = 600 rpm

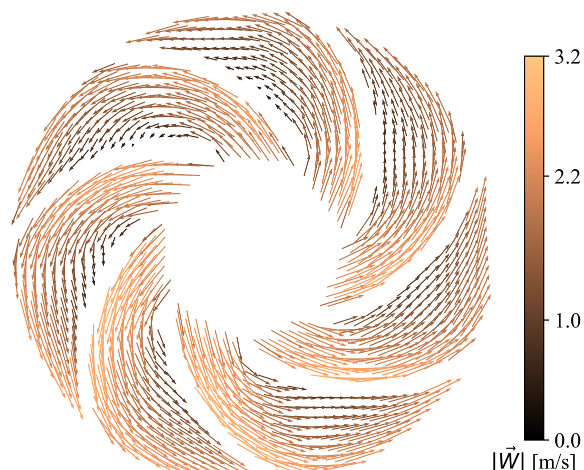

(f) Q_w = 1.6 Q_{BEP} at N = 900 rpm

Fig. 6 Average relative velocity W_{center} measured on the central plane of the impeller.

(a) Q_w = 0.1 Q_{BEP} measured next to hub plane

(b) Q_w = 0.1 Q_{BEP} measured next to shroud plane

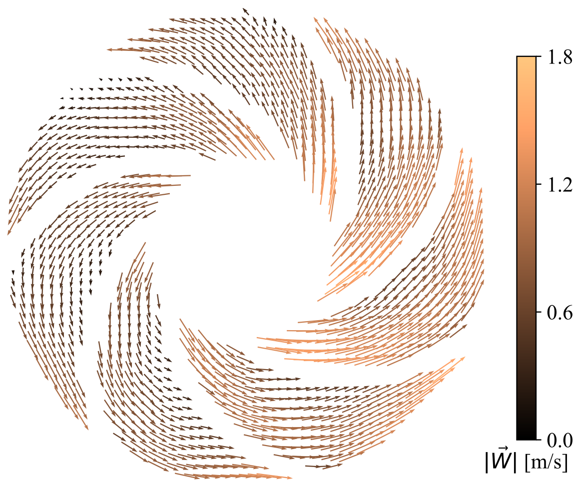

(c) Q_w = 1.0 Q_{BEP} measured next to hub plane

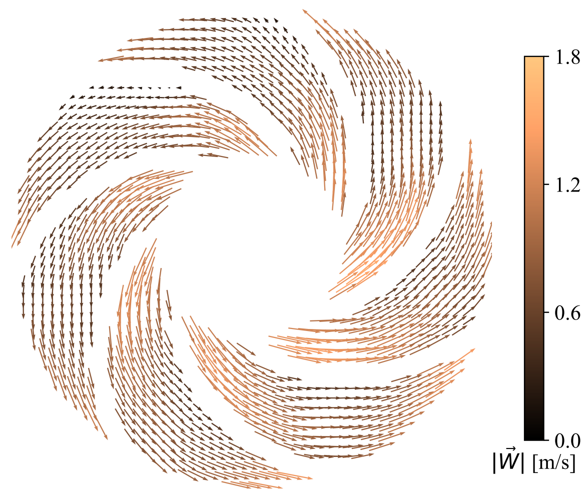

(d) Q_w = 1.0 Q_{BEP} measured next to shroud plane

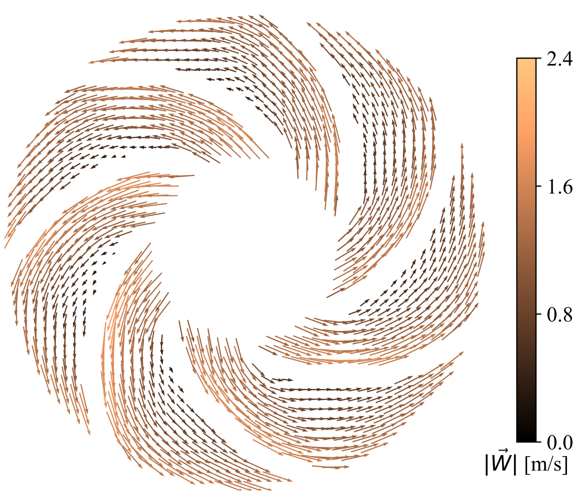

(e) Q_w = 1.6 Q_{BEP} measured next to hub plane

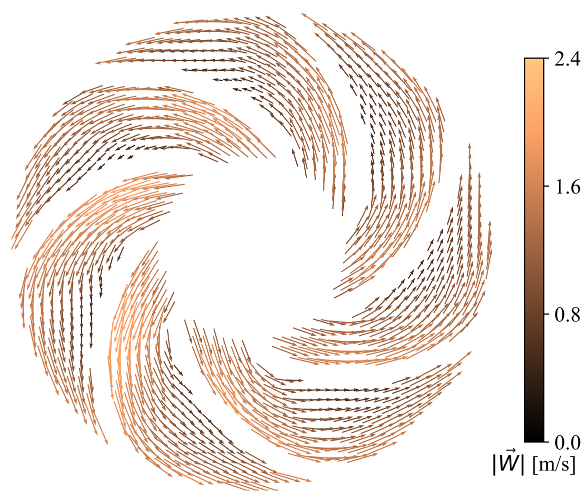

(f) Q_w = 1.6 Q_{BEP} measured next to shroud plane

Fig. 7 Average relative velocity W_{hub} and W_{shroud}, measured on peripheral planes, at N = 600 rpm.

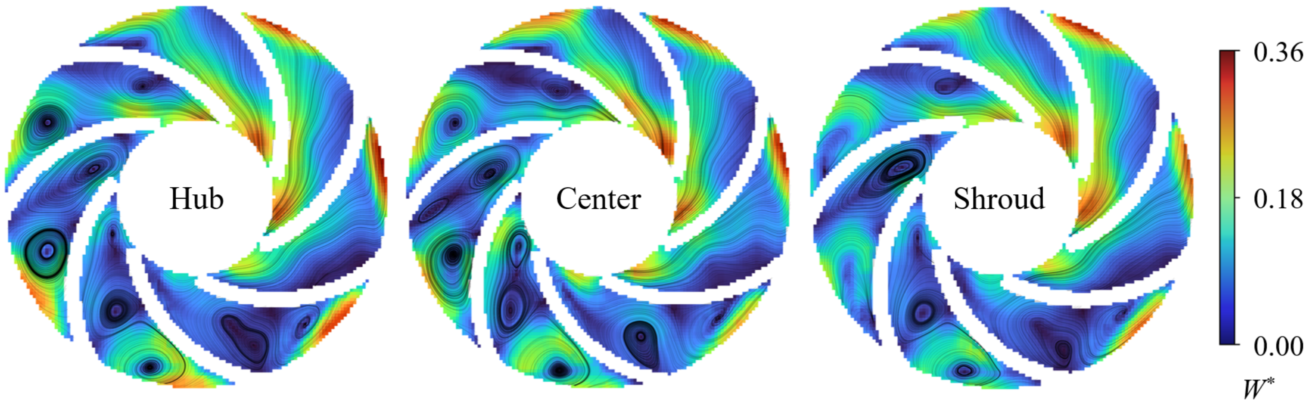

(*a*) $Q_w = 0.1\ Q_{BEP}$, measurements performed on three axial planes

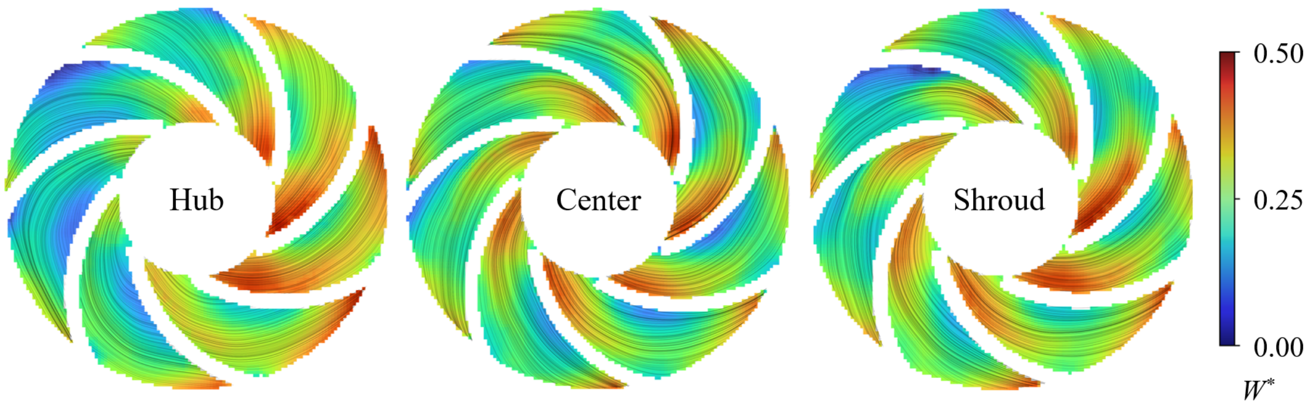

(*b*) $Q_w = 1.0\ Q_{BEP}$, measurements performed on three axial planes

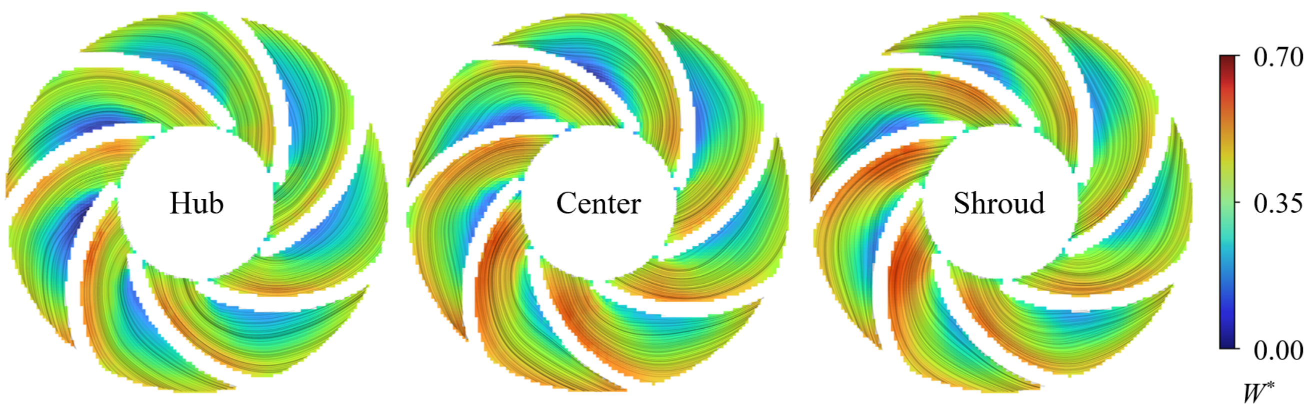

(*c*) $Q_w = 1.6\ Q_{BEP}$, measurements performed on three axial planes

Fig. 8 Streamlines superimposed on contour plots of normalized relative velocity, $W^* = W/(\Omega r_2)$, measured on the central and peripheral planes in the impeller and volute. N = 600 rpm.

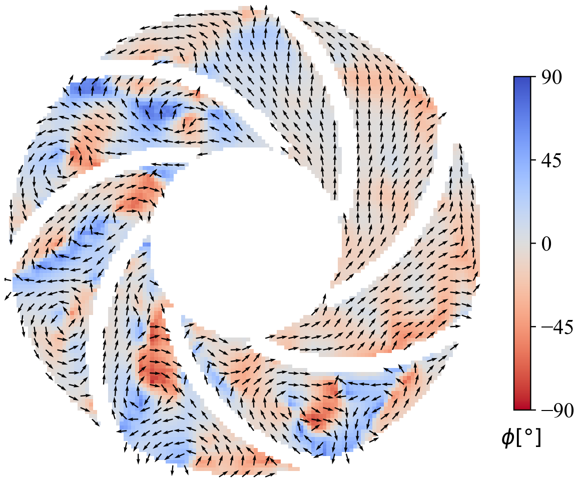

(*a*) Q_w = 0.1 Q_{BEP} measured next to hub plane

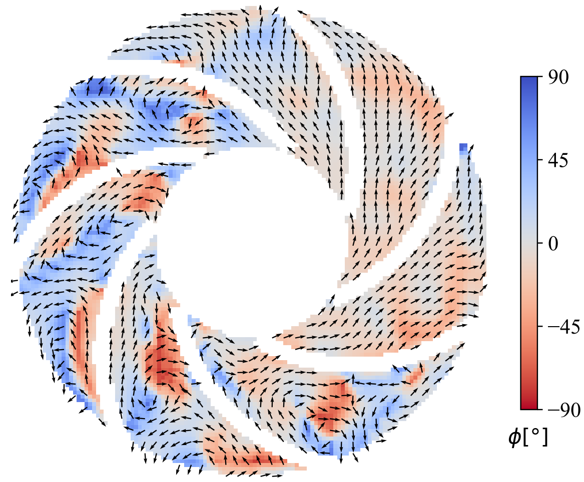

(*b*) Q_w = 0.1 Q_{BEP} measured next to shroud plane

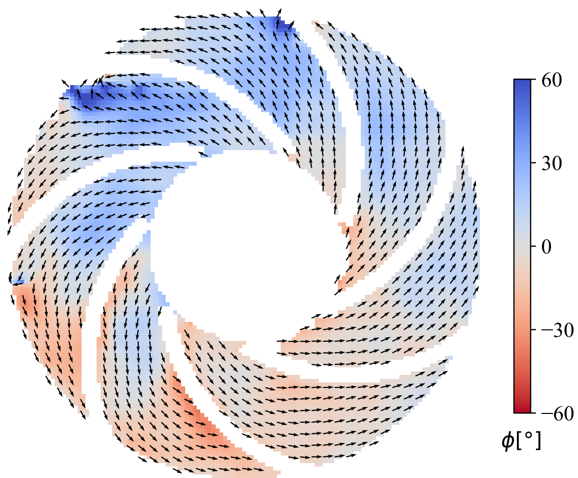

(*c*) Q_w = 1.0 Q_{BEP} measured next to hub plane

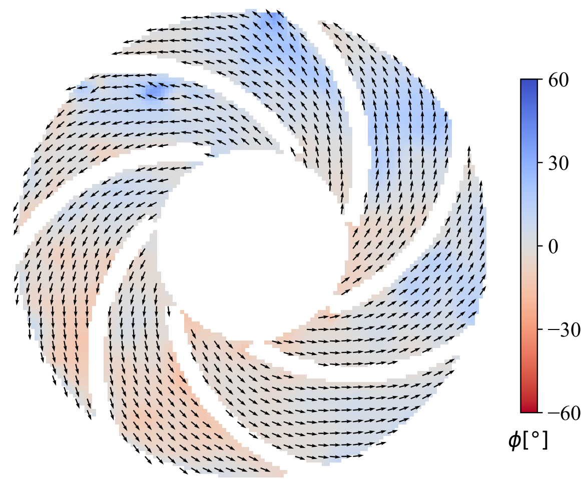

(*d*) Q_w = 1.0 Q_{BEP} measured next to shroud plane

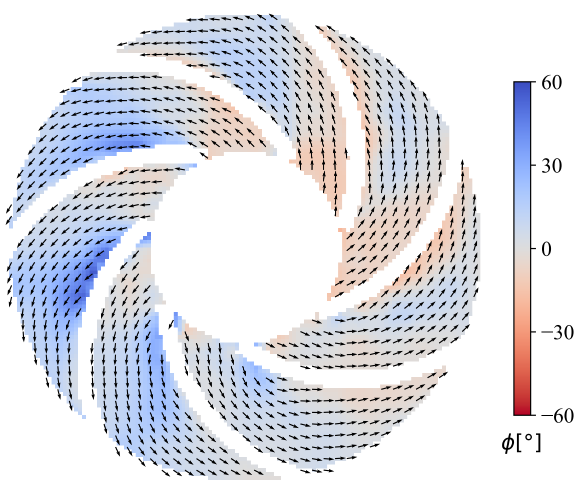

(*e*) Q_w = 1.6 Q_{BEP} measured next to hub plane

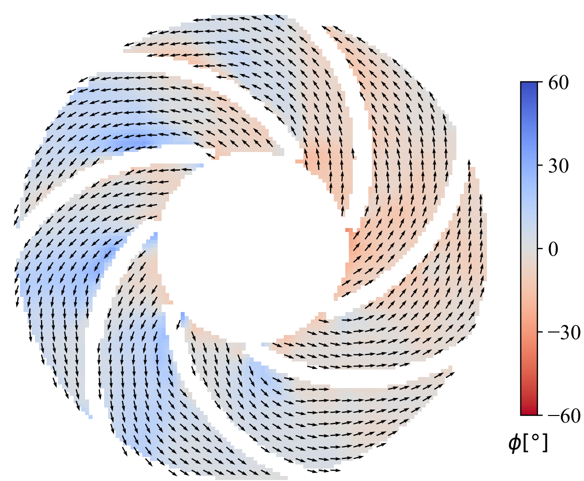

(*f*) Q_w = 1.6 Q_{BEP} measured next to shroud plane

Fig. 9 Angle of deviation ϕ between central and peripheral velocity vectors for N = 600 rpm.

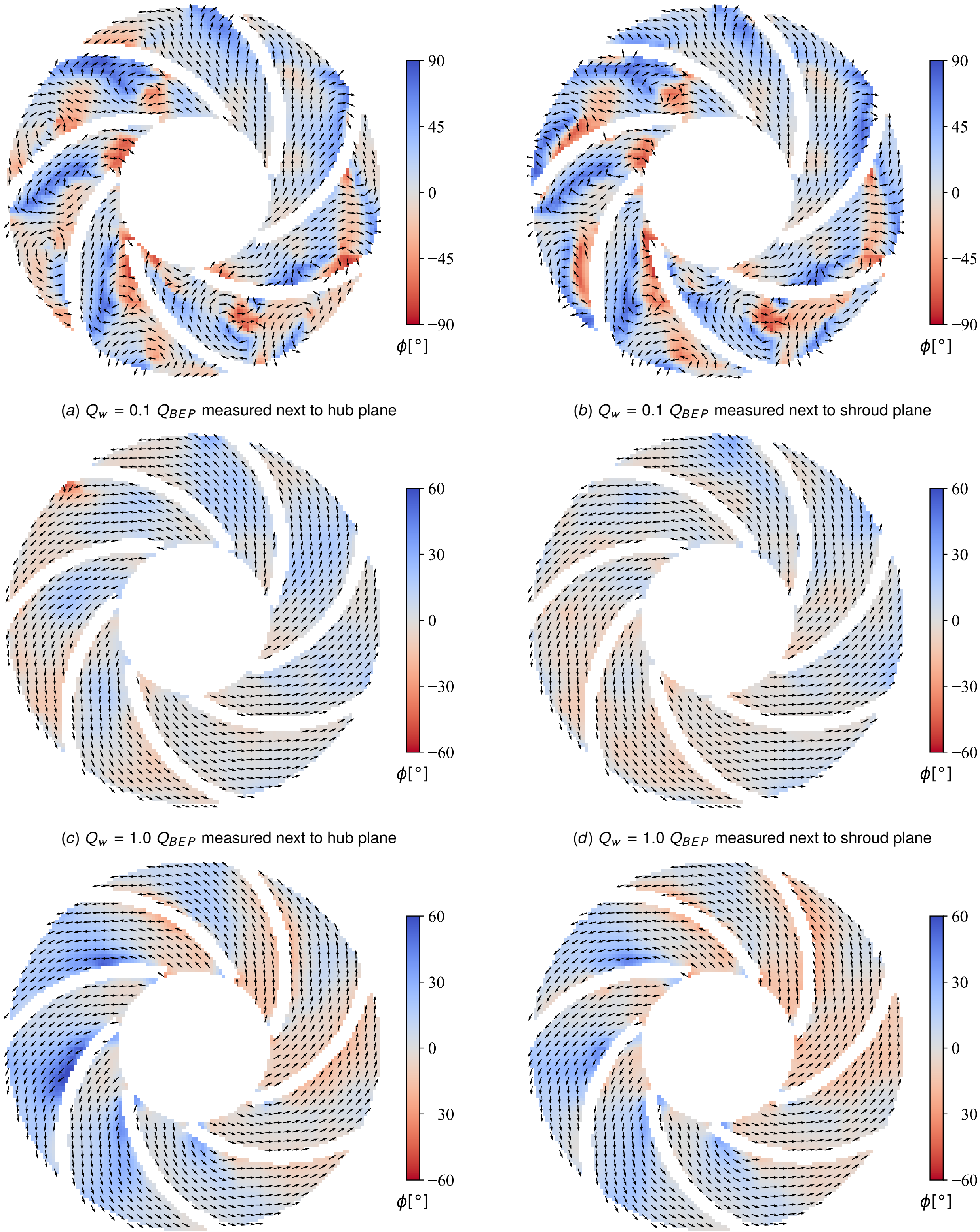

(*a*) $Q_w = 0.1\ Q_{BEP}$ measured next to hub plane

(*b*) $Q_w = 0.1\ Q_{BEP}$ measured next to shroud plane

(*c*) $Q_w = 1.0\ Q_{BEP}$ measured next to hub plane

(*d*) $Q_w = 1.0\ Q_{BEP}$ measured next to shroud plane

(*e*) $Q_w = 1.6\ Q_{BEP}$ measured next to hub plane

(*f*) $Q_w = 1.6\ Q_{BEP}$ measured next to shroud plane

Fig. 10 Angle of deviation ϕ between central and peripheral velocity vectors for N = 900 rpm.

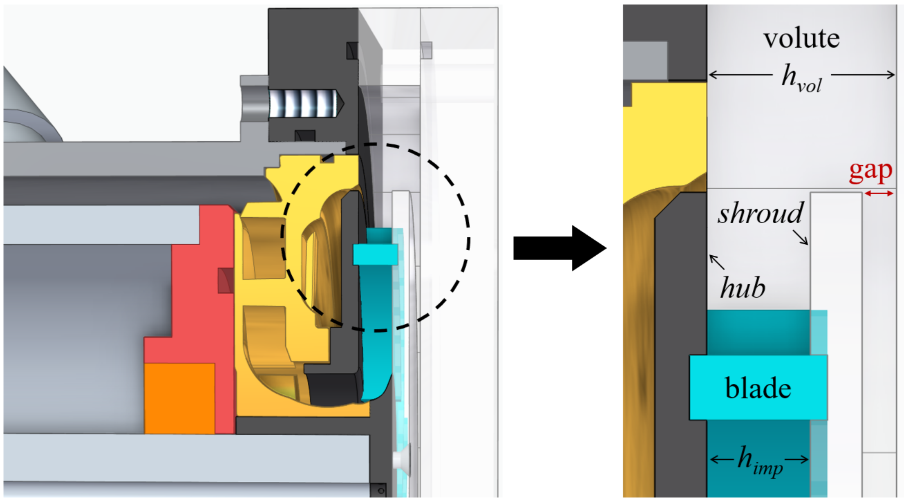

Fig. 11 Technical drawing of the pump stage. Cutaway view highlighting the impeller assembled in the volute.

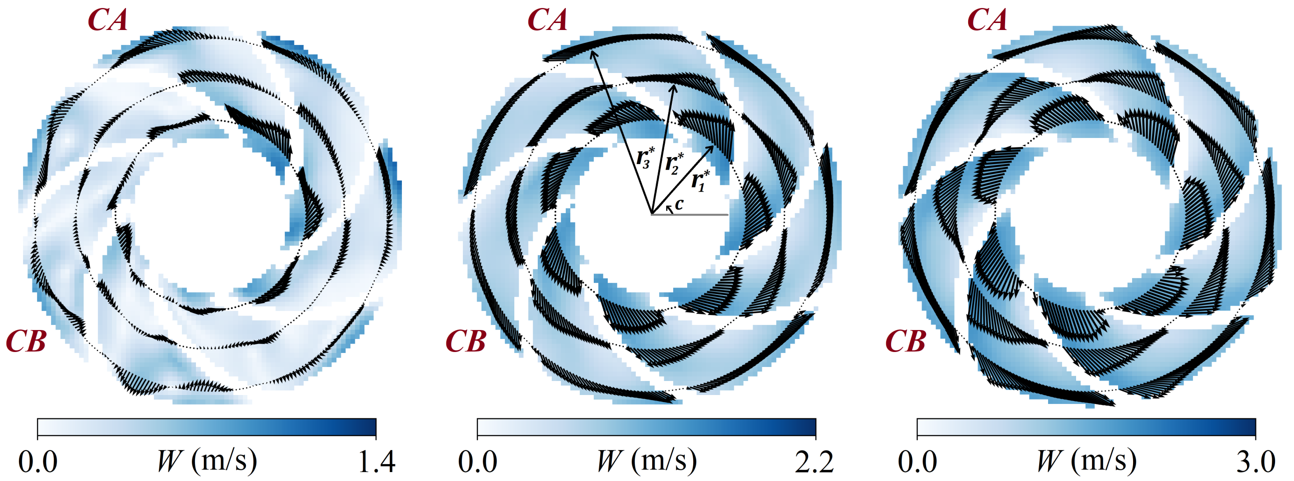

(*a*) $Q_w = 0.1\ Q_{BEP}$ (*b*) $Q_w = 1.0\ Q_{BEP}$ (*c*) $Q_w = 1.6\ Q_{BEP}$

Fig. 12 Velocity vectors $\mathbf{W}_{center}$ (black) superimposed on velocity magnitudes W_{center} (blue) in the 3 radial positions $r^* = r/r_2 = [0.5, 0.7, 0.9]$ for N = 600 rpm. In this example, measurements refer to the central plane of the impeller.

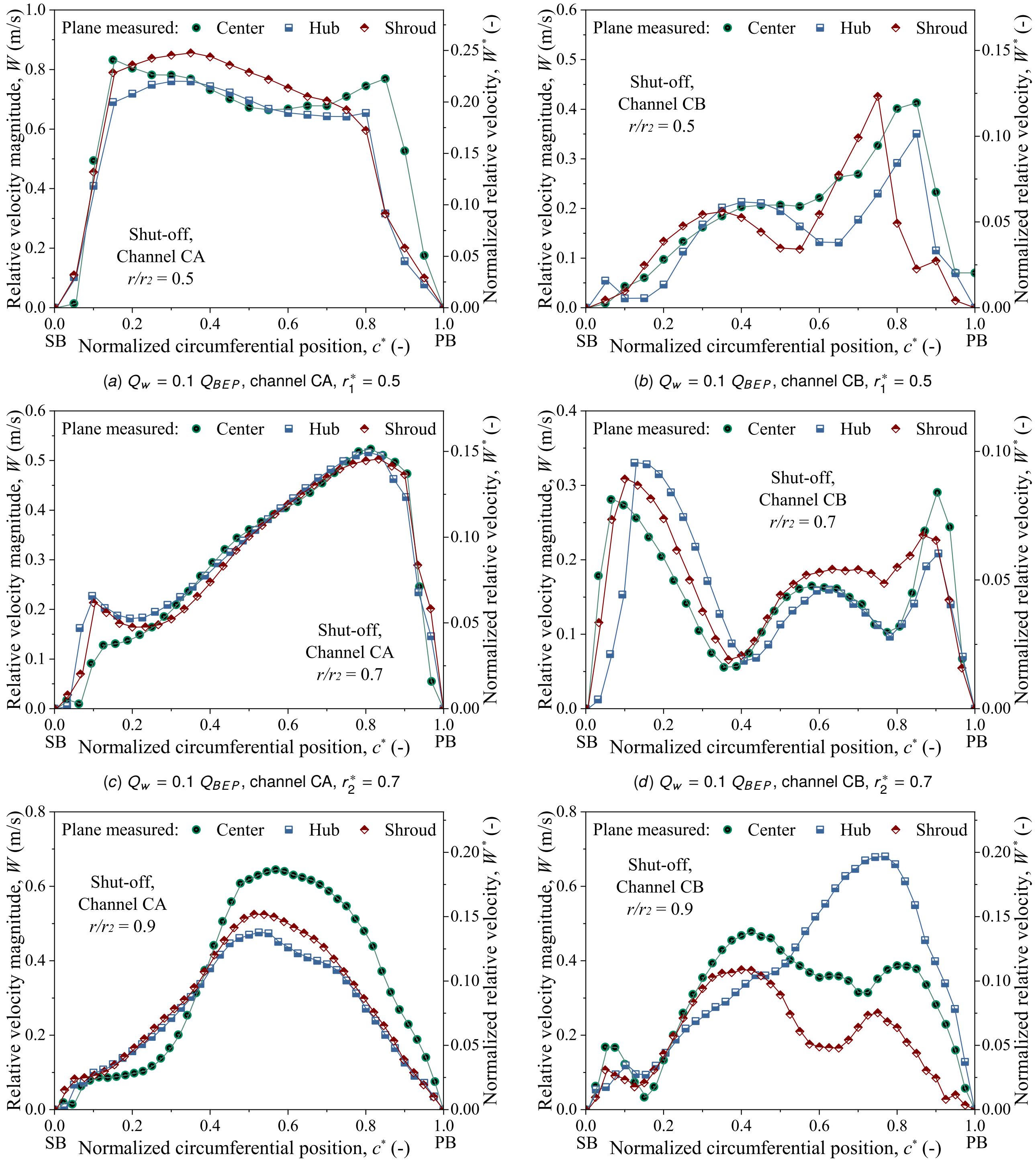

(*a*) Q_w = 0.1 Q_{BEP}, channel CA, r_1^* = 0.5

(*b*) Q_w = 0.1 Q_{BEP}, channel CB, r_1^* = 0.5

(*c*) Q_w = 0.1 Q_{BEP}, channel CA, r_2^* = 0.7

(*d*) Q_w = 0.1 Q_{BEP}, channel CB, r_2^* = 0.7

(*e*) Q_w = 0.1 Q_{BEP}, channel CA, r_3^* = 0.9

(*f*) Q_w = 0.1 Q_{BEP}, channel CB, r_3^* = 0.9

Fig. 13 Profiles of relative velocity, W, and normalized relative velocity, W^*, measured next to central and peripheral planes in the impeller. Shut-off condition at N = 600 rpm.

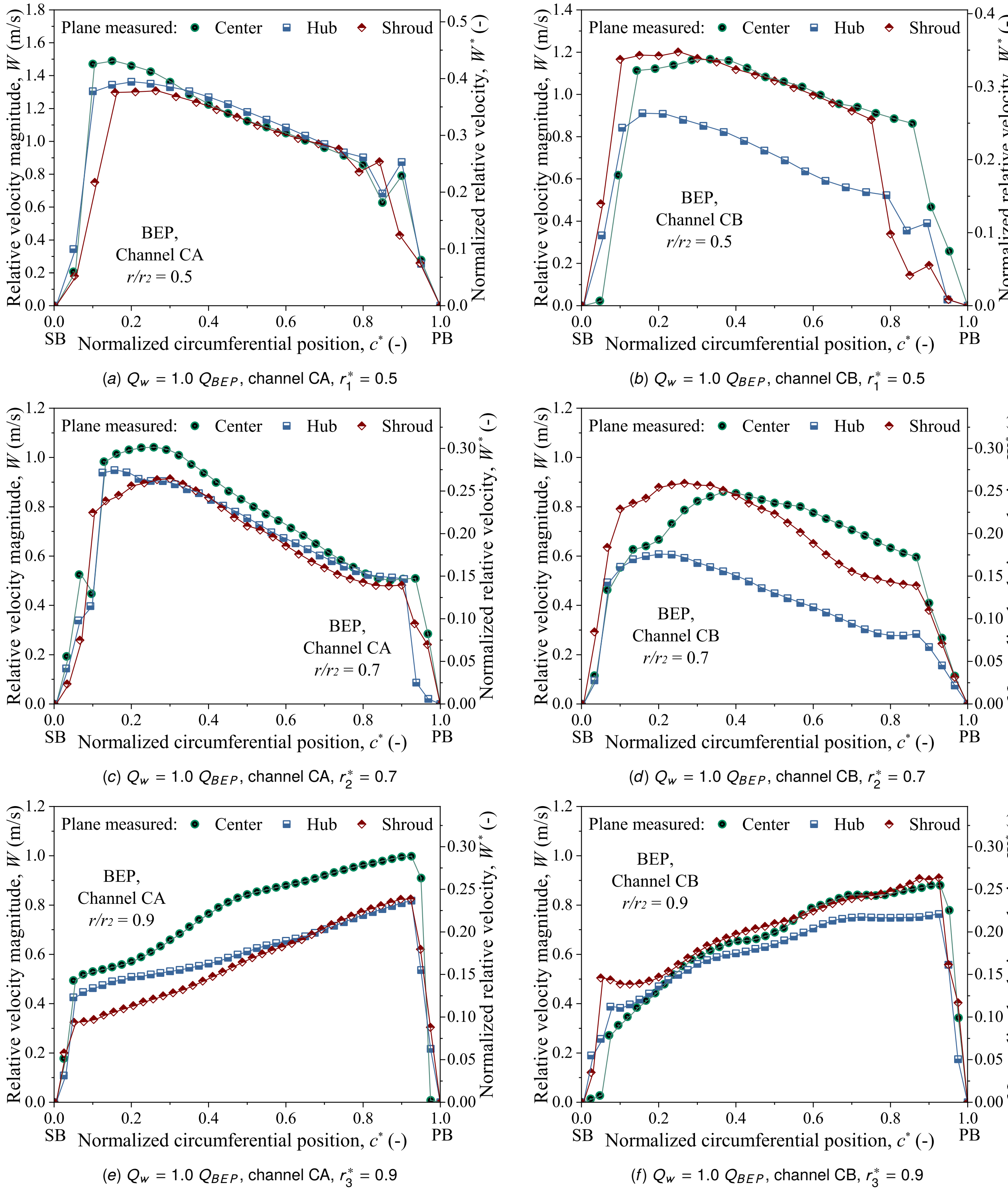

Fig. 14 Profiles of relative velocity, W, and normalized relative velocity, W^*, measured next to central and peripheral planes in the impeller. BEP condition at N = 600 rpm.

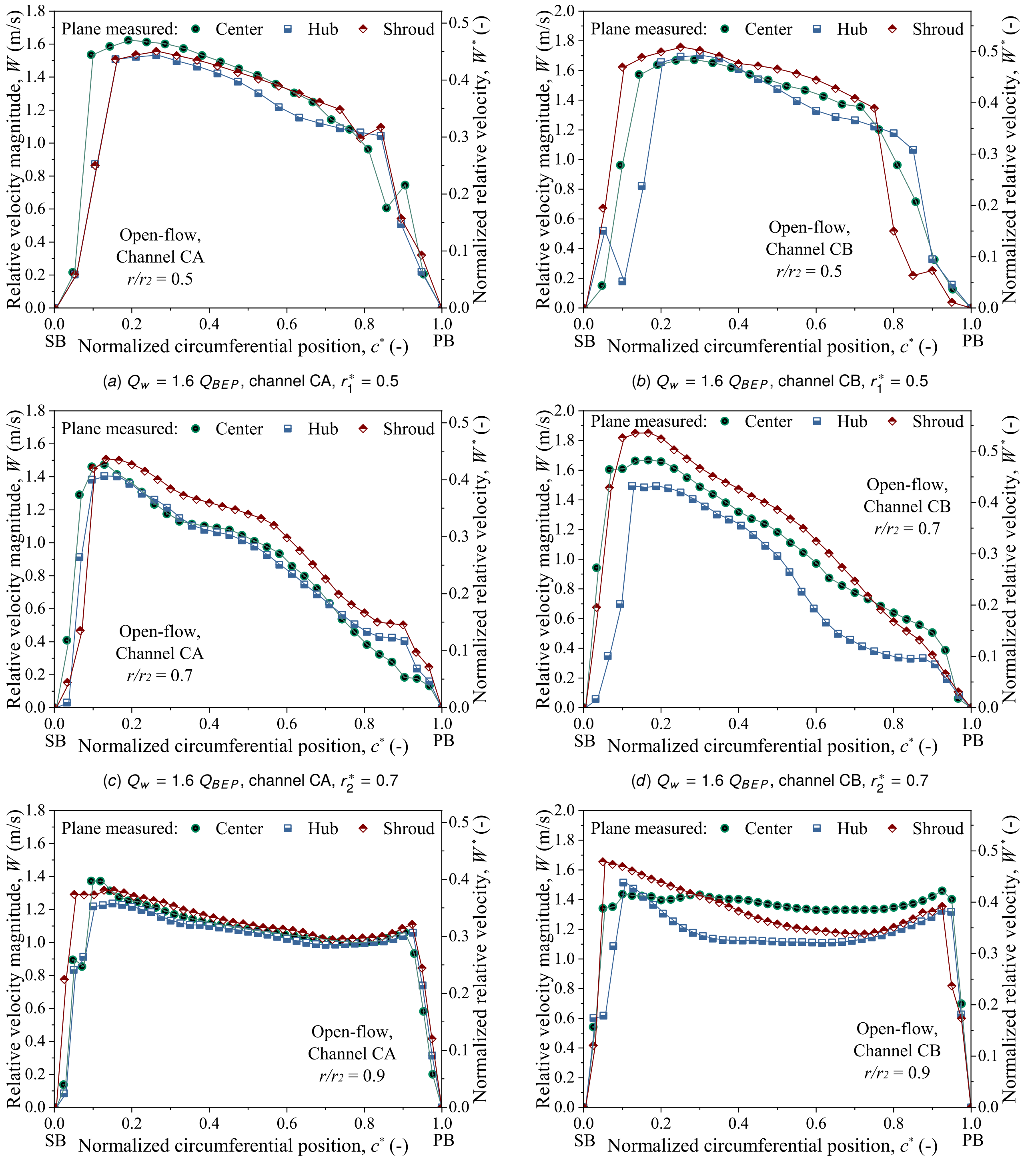

(*a*) $Q_w = 1.6\ Q_{BEP}$, channel CA, $r_1^* = 0.5$

(*b*) $Q_w = 1.6\ Q_{BEP}$, channel CB, $r_1^* = 0.5$

(*c*) $Q_w = 1.6\ Q_{BEP}$, channel CA, $r_2^* = 0.7$

(*d*) $Q_w = 1.6\ Q_{BEP}$, channel CB, $r_2^* = 0.7$

(*e*) $Q_w = 1.6\ Q_{BEP}$, channel CA, $r_3^* = 0.9$

(*f*) $Q_w = 1.6\ Q_{BEP}$, channel CB, $r_3^* = 0.9$

Fig. 15 Profiles of relative velocity, W, and normalized relative velocity, W^*, measured next to central and peripheral planes in the impeller. Open-flow condition at $N = 600$ rpm.

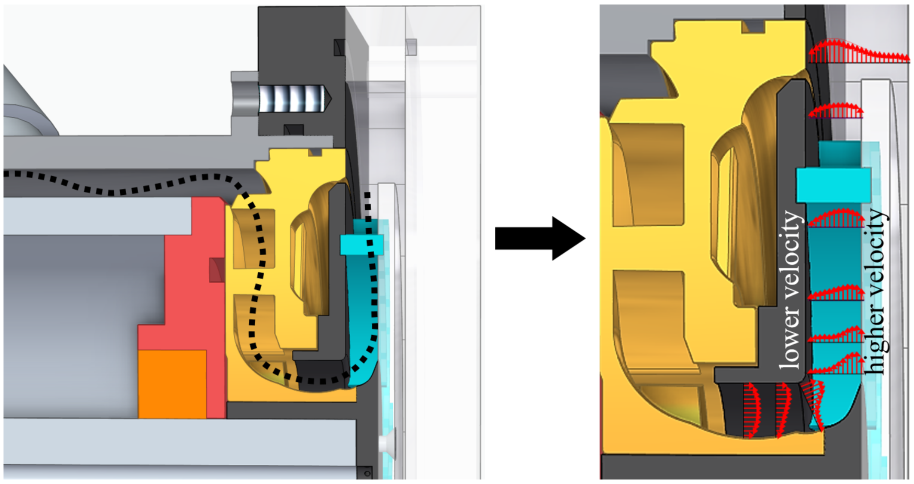

Fig. 16 Cutaway view of the pump. The fluid path (left) undergoes a change in its direction before entering the impeller. This fact causes the velocity profiles (right) to become distorted. Note: the profiles are purely illustrative.

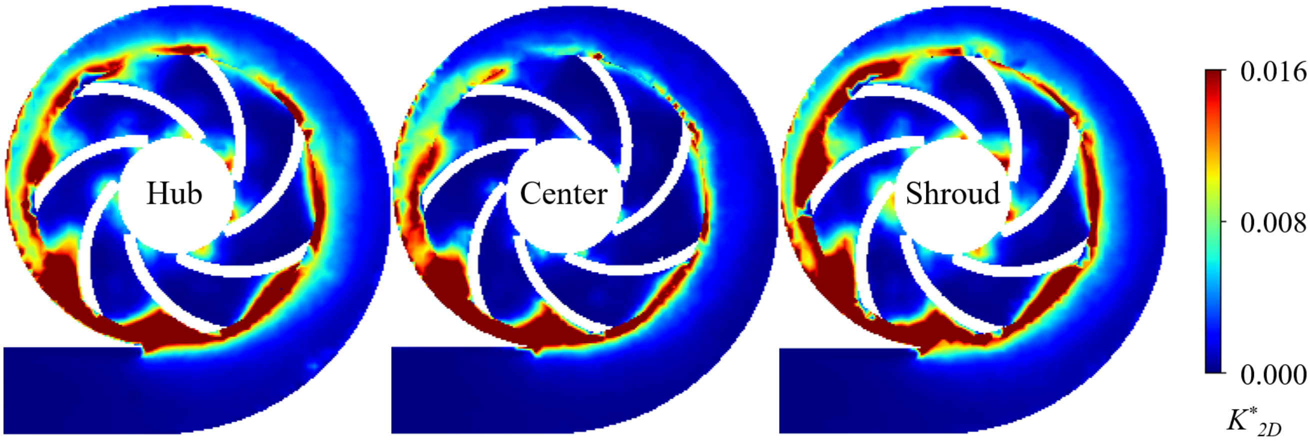

(a) $Q_w = 0.1\ Q_{BEP}$, measurements performed on three axial planes

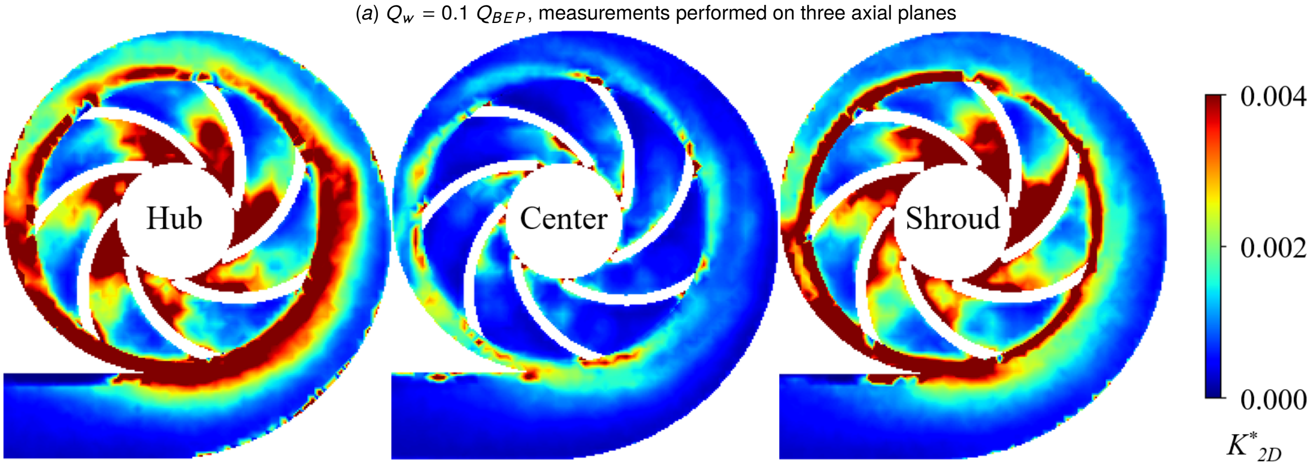

(b) $Q_w = 1.0\ Q_{BEP}$, measurements performed on three axial planes

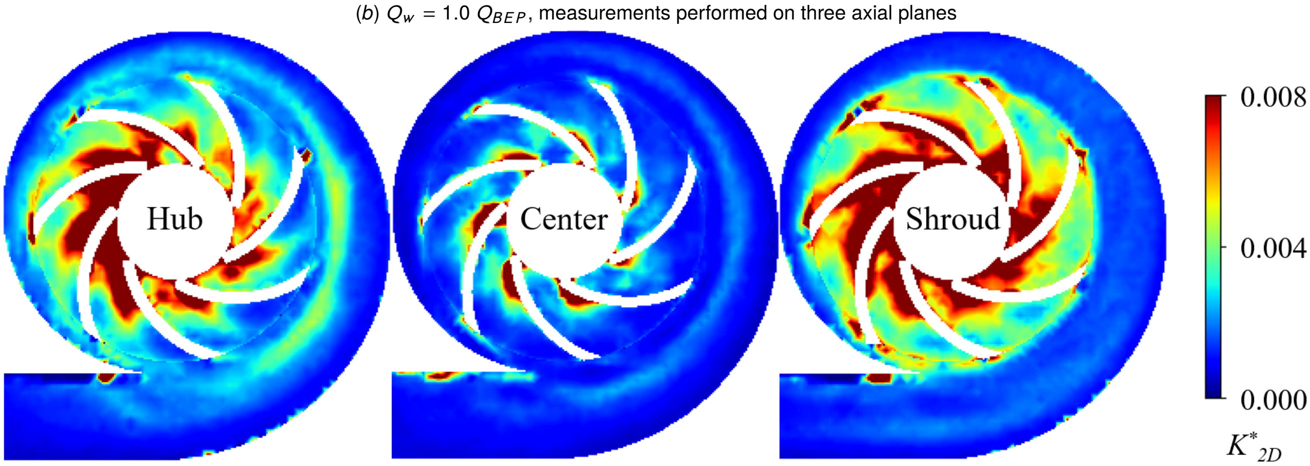

(c) $Q_w = 1.6\ Q_{BEP}$, measurements performed on three axial planes

Fig. 17 Contour plots of normalized turbulent kinetic energy, K^{*}_{2D}, measured on the central and the peripheral planes in the impeller and volute. N = 600 rpm.

,

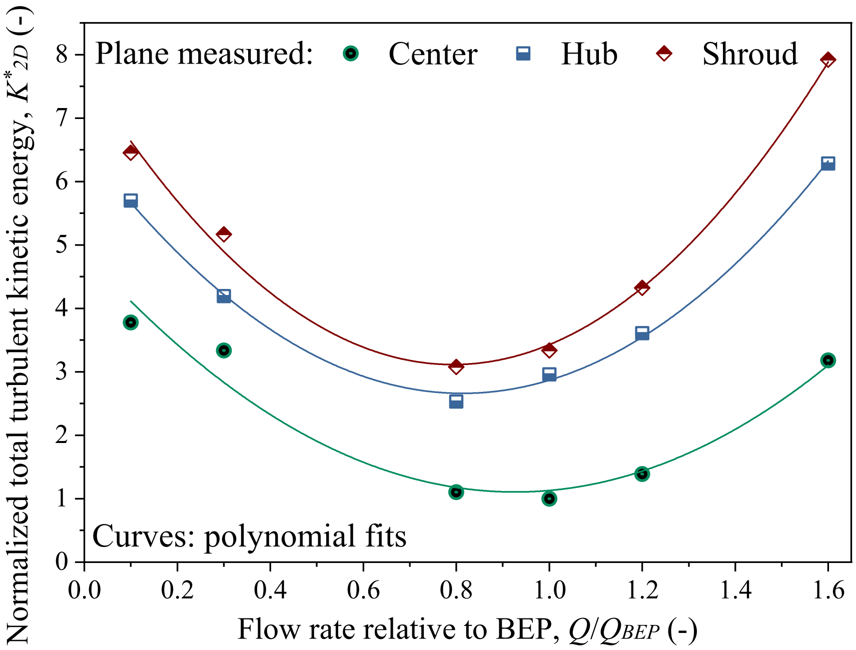

Fig. 18 Total turbulent kinetic energy in the entire impeller, on three planes and six flow rates. N = 600 rpm.